This article has been accepted for publication in a future issue of this journal, but has not been fully edited. Content may change prior to final publication. Citation information: DOI 10.1109/TMI.2015.2474119, IEEE Transactions on Medical Imaging

Lung lesion extraction using a toboggan based growing automatic segmentation approach

Jiangdian Song, Caiyun Yang, Li Fan, Kun Wang, Feng Yang, Shiyuan Liu*, Jie Tian*, *Fellow, IEEE*

***Abstract*—The accurate segmentation of lung lesions from computed tomography (CT) scans is important for lung cancer research and can offer valuable information for clinical diagnosis and treatment. However, it is challenging to achieve a fully automatic lesion detection and segmentation with acceptable accuracy due to the heterogeneity of lung lesions. Here, we propose a novel toboggan based growing automatic segmentation approach (TBGA) with a three-step framework, which are automatic initial seed point selection, multi-constraints 3D lesion extraction and the final lesion refinement. The new approach does not require any human interaction or training dataset for lesion detection, yet it can provide a high lesion detection sensitivity (96.35%) and a comparable segmentation accuracy with manual segmentation ($P > 0.05$), which was proved by a series assessments using the LIDC-IDRI dataset (850 lesions) and in-house clinical dataset (121 lesions). We also compared TBGA with commonly used level set and skeleton graph cut methods, respectively. The results indicated a significant improvement of segmentation accuracy ($P < 0.05$). Furthermore, the average time consumption for one lesion segmentation was under 8 seconds using our new method. In conclusion, we believe that the novel TBGA can achieve robust, efficient and accurate lung lesion segmentation in CT images automatically.**

***Index Terms*—Back-off mechanism, computed tomography (CT), lung lesion segmentation, region growing, toboggan.**

This paper is supported by the Chinese Academy of Sciences Key Deployment Program under Grant No. KGZD-EW-T03, the National Basic Research Program of China (973 Program) under Grant 2011CB707700, the National Natural Science Foundation of China under Grant Nos. 81227901, 61231004, 81370035, 81230030, 61301002, 61302025, major projects of Biomedicine Department of Shanghai Science and Technology Commission (13411950100), the Chinese Academy of Sciences Fellowship for Young International Scientists under Grant 2013Y1GB0005, the National High Technology Research and Development Program of China (863 Program) under 2012AA021105, the "Guangdong Province-Chinese Academy of Sciences" comprehensive strategic cooperation program under 2010A090100032 and 2012B090400039, the NSFC-NIH Biomedical collaborative research program under 81261120414, the National Science and Technology Supporting Plan under 2012BAI15B08, the Beijing Natural Science Foundation under Grant No. 4132080, the Fundamental Research Funds for the Central Universities under Grant No. 2013JBZ014, and the Chinese Academy of Sciences Visiting Professorship for Senior International Scientists under Grant 2010T2G36. *Asterisk indicates corresponding author.*

J. Song is with the Sino-Dutch Biomedical and Information Engineering School, Northeastern University, Shenyang, 110819, China. And the Key Laboratory of Molecular Imaging, Institute of Automation, Chinese Academy of Sciences, Beijing 100190, China.

*C. Yang, K. Wang and *J. Tian is with the Key Laboratory of Molecular Imaging, Institute of Automation, Chinese Academy of Sciences, Beijing 100190, China.

L. Fan and *S. Liu is with the Department of Radiology, Changzheng Hospital, Second Military Medical University, Shanghai, 200003, China.

F. Yang is with the Beijing Jiaotong University, Beijing, 100044, China.

I. Introduction

LUNG cancer is the leading cause of cancer mortality around the world [1]. Up to 10 million patients in the world will die of lung cancer by 2030 in terms of the report from the World Health Organization [2]. Early prevention of lung tumor has an important role for survival benefit improvements. With the hypothesis that deep analysis of radiographic images can inform and quantify the microenvironment and the extent of intra-tumoral heterogeneity for personalized medicine [3][4], analysis of large numbers of image features extracted from computed tomography (CT) with high throughput can capture spatial and temporal genetic heterogeneity in a non-invasive way, which is better than invasive biopsy based molecular assays. It will be useful for medical research, computer-aided diagnosis, radiotherapy and evaluations of surgery outcome as well. For this purpose, accurate segmentation of lung lesions is the pre-requisite. One method for lung lesion segmentation is that experts with experience such as radiologists delineate the lesion manually. It is a difficult task to obtain robust and efficient results for a variety of reasons. First, the experts may overestimate the lesion volume to enclose the whole lesion. Different manual delineations are also varying. Furthermore, the time consumption limits converting CT images to mineable data with high throughput. Therefore a highly robust, efficient and automatic lung lesion segmentation approach is urgently required.

However, accurate segmentation of lung lesions by an automatic method is also difficult because the heterogeneity of the lesions. As shown in Fig 1, due to the diversity of lung lesions, current segmentation accuracy is inadequate. The shape, intensity and location of lung lesions change greatly because of the existence of the spatial genetic heterogeneity of various lesions. The intensity of lung lesions is sometimes close to the intensity of vessels, fissures or chest wall (Fig. 1 a(1)-a(3)). But other times it is close to the intensity of lung field, such as ground-glass opacity (GGO) (Fig. 1 c(1)-c(3)), which is a nonspecific finding on CT scans that indicates a partial filling of air spaces by exudate or transudate, as well as interstitial thickening or partial collapse of lung alveoli [5]. Moreover, the influence of the inherent noise in CT images can also be significant. All these facts render that it is very challenging to achieve the precise delineation of lung lesions automatically.

This article has been accepted for publication in a future issue of this journal, but has not been fully edited. Content may change prior to final publication. Citation information: DOI 10.1109/TMI.2015.2474119, IEEE Transactions on Medical Imaging

A. Related work

Based on the CT data of lung, many researchers have done relevant works to pulmonary parenchyma, airway [6]-[8] and lung lesion segmentation. Campos et al. [9] proposed a supervised lung nodule segmentation method via volumetric shape index, convergence index filter and k-Nearest Neighbor (k-NN) regression to gain three coarse segmentation results. A feature based two layer supervised learning method for nodule classification was used simultaneously. Then, a refining method by the artificial neural network (ANN) was used to segment the lung nodules. The result showed that they could receive 12% relative volume error for GGO. However, the three preliminary segmentations they used to obtain a feature set were time-consuming. Another problem was their segmentation needs human interaction for the initial seed point. Diciotti et al. divided the lesions into "well circumscribed" and "juxta-vascular" groups in [10], where they obtained a detection sensitivity of 85.3% on the Lung Image Database Consortium (LIDC-IDRI) dataset, which contains 23 lesions at that time. The dataset has been expanded to 1010 cases now [11], and widely used to evaluate lung lesion segmentation methods, as an internationally recognized lung lesion database. In [12], a local shape analysis method for small lung nodule segmentation was used on the juxta-vascular and juxta-pleural lesions, and a detection sensitivity of 88.5% was reported on 157 lesions from the LIDC-IDRI database. In Wu and Lu's work [13], a system based on the conditional random field model which integrated texture, grayscale, shape and curvature was built to provide a reasonable segmentation input for the subsequent classification. The authors also used probability response maps and pairwise probability co-occurrence maps to find the contextual correlation of nodules. However, the co-occurrence matrix emphasizes image texture among pixels rather than pixel intensity information itself. As a result, it is not applicable for weak texture lesions. A novel level set approach for lung nodule segmentation was proposed in [14], and a detection sensitivity of 94.3% was received by a dataset which included 742 lung lesions. Another method concentrated on juxta-vascular lesion segmentation based on flow entropy and geodesic distance was represented in [15], which obtained a detection sensitivity of 91.7% on 157 lesions from the LIDC-IDRI database. Recently, an automated delineation method of lung tumors using the single click ensemble segmentation approach (SCES) has been applied for solid tumor extraction [16]. The work was built on a lung tumor analysis tool [17] within the Definiens Cognition Network Technology developed by Definiens AG [18] and Merck & Co., Inc. which could provide a fast and easy annotation of lung lesions or other user-defined regions of interest. Compared with manual segmentation, an accuracy of 78.72% was received by SCES, although one human interaction was needed. A new dynamic programming and multi-direction fusion technique were presented in [19]. The first dataset (23 lesions) and second dataset (64 lesions) from the LIDC-IDRI were both used to verify the new approach, and 75% segmentation accuracy was acquired. Another research for lung lesion segmentation was proposed by Kubota [20]. A convexity model with morphological method was used to deal with the intensity heterogeneity in lung lesions. To evaluate the algorithm, 105 lesions from the LIDC-IDRI database were used and 69% segmentation accuracy was obtained. In [21], the authors tried to present a new pathological lung segmentation approach to detect all abnormal imaging patterns such as consolidations, nodules, ground-glass opacities and honeycombs. In this research, fuzzy connectedness and rib-cage were used to estimate the lung volume. This study could delineate most types of lung lesions. However, the authors only presented the accuracy of lung field segmentation; the similarity of their lesion segmentation results with the published manual segmentation standard was not discussed.

In order to make the lung lesion segmentation fully automatic, it is necessary to develop an automatic and accurate method for the seed point selection. As the precursor of lesion detection, methods for 3D lung volume segmentation have been provided in [22] and [23], which the measurement error was less than a pixel when compared with human analysis. In addition, the accuracy of 90% for lung volume segmentation and 89% of lesion detection sensitivity have been reported in [24]-[26] by pixel intensity features and texture features. Recently, a large-scale lung cancer screening study including more than 3000 lesions was used for pulmonary nodule detection in [27]. Lesion curvedness and phenotype descriptors were used for seed point selection in each lesion cluster. Then, k-nearest neighbors (K-NN) clustering with multi-features was applied to reduce false positives. In [28], lesion candidate masks were extracted from 15 thresholds with the opening operation. Then, phenotypic features were used for pulmonary nodule recognition. However, the later segmentation only achieved 63% accuracy, which is relatively poor. A nodule detection method using isosurface triangulation with varying thresholds and phenotypic features was presented to detect lesions in [29]. Based on the self-organizing maps (SOMs) and artificial neural networks (ANNs) classification, this method obtained a detection sensitivity of 80% on CT images from the LIDC-IDRI. Divergence and multi-scale enhancement filters for nodule clustering were used in [30]. A genetic algorithm and ANNs were the final classifiers for false positive elimination, and a detection sensitivity of 87.5% with an average of four false positives per scan was achieved. All of the methods mentioned above provide feasible ways for lung lesion detection, but they require nodule candidate preprocessing, such as down-sampling, contrast enhancement and entire lung volume segmentation. Besides, different classifiers using a large number of training datasets, and phenotypic features are also needed for false positive reduction. Finally, the number of human interactions in those methods is also not clear. To provide fast, accurate and reliable lung lesion detection and segmentation for clinical aided diagnosis and other potential applications, we present a new method to address the above issues.

This article has been accepted for publication in a future issue of this journal, but has not been fully edited. Content may change prior to final publication. Citation information: DOI 10.1109/TMI.2015.2474119, IEEE Transactions on Medical Imaging

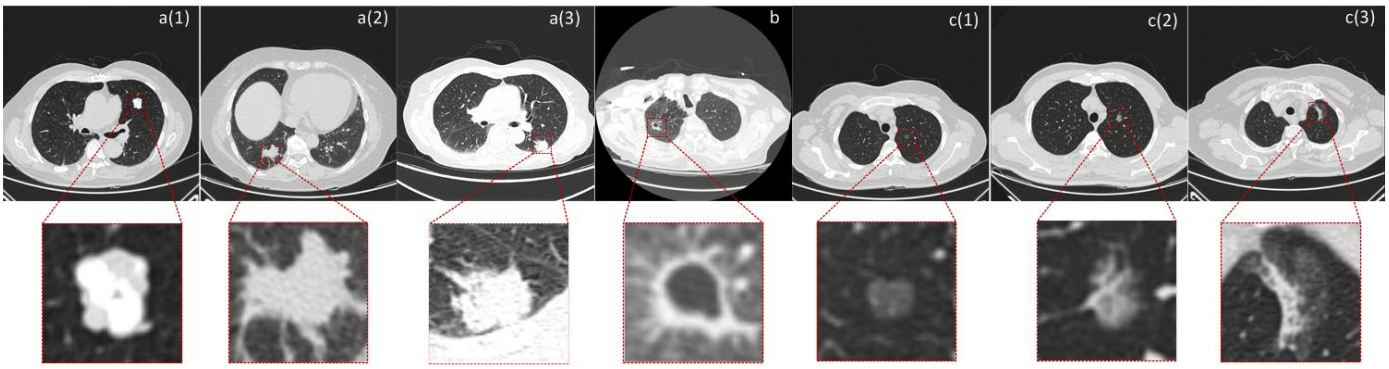

Fig. 1. Different types of lung lesions: (a1)-(a3): solid nodule, a(1): solitary nodule, a(2): juxta-vascular, a(3): juxta-pleural, (b): cavity, (c1)-(c3): GGO. c(1): solitary, c(2): juxta-vascular, c(3): juxta-pleural.

This paper proposes a novel lung lesion seed point detection method based on the toboggan algorithm to achieve automatic selection of the lesion seed point, which is on demand in many lesion segmentation problems. The toboggan method has been widely used for image segmentation [31]-[35], but the research using it for automatic selection of the lesion seed point in medical images is rare. From a number of experiments on different lung images, we find that the toboggan method is a potential way for lung lesion seed point selection. The algorithm proposed in this paper gives a new advanced toboggan method applied to seed point detection for solid nodules, ground-glass opacities and cavities. As the first step of our method (denoted by TBGA), lesion seed points are obtained from the gradient image of the pulmonary parenchyma (lesion contained) by the new toboggan method. Then, an iterative growing method with distance constraint and "growing degree" constraint are applied for lesion segmentation. Finally, we present a lung lesion refining method by the contour of the segmented lesion to eliminate the vessels and other tissues included as lung lesion in the previous segmentation. Through massive experiments, we demonstrate that the new method not only avoids manual participation and hundreds of training datasets for lesion detection, but also provides accurate and robust results for different types of lung lesions (solitary, juxta-pleural and juxta-vascular lesions).

B. Our contributions

The key findings of our study in this paper include the following three aspects. First, the proposed three step framework for lung lesion segmentation is fully-automatic without using any training datasets or human interventions. Second, the new approach works well not only for solid nodules but also for GGO. Finally, better performance is obtained with improved time efficiency through the comparison with other lung lesion extraction algorithms.

The paper is organized as follows. Detailed description of the segmentation framework of TBGA is presented in Section II, which contains the automatic selection of lesion seed points (Section II-A and II-B), 3D lesion segmentation (Section II-C), and the final lesion refinement (Section II-D). Section III provides multi-methods comparison based one public and one in-house clinical dataset. The accuracy, sensitivity and efficiency of the new method are demonstrated. The overall performance and limitations of TBGA is discussed in Section IV, and the final conclusion is shown in Section V.

II. METHODS

The proposed method consists of three phases: seed selection, lesion extraction and lesion refining. Fig. 2 presents the overview of the proposed method. A more detailed flowchart with figures for each step has been appended to this paper. The input of our algorithm is a slice of CT image containing lung lesion(s). For the first step, the algorithm proposed in [36] is applied to segment the lung parenchyma automatically. The segmented lung is shown in Fig. 3(a). After that, a multi-scale Gaussian filter is applied to compute the gradient magnitude of each pixel in this lung parenchyma image. Then, the improved toboggan algorithm is applied to the gradient image of lung parenchyma to detect the four-connected neighborhoods around each pixel for a destination pixel with the minimum gradient value. A unique mark will be targeted on the original pixel once its minimum is found. After all of the pixels are labeled, those highlighted parts in the original lung parenchyma image such as vessels and noise will be moved to the lower gray part (lung field) while the lesion is still highlighted. It means that only the lesion is left for automatic seed point selection and other parts such as vessels are excluded. As lung nodules are observed to have spherical shape but vessels have anisotropic shape, the elongated morphological characteristic of vessels is mainly responsible for its elimination. All the process in the first step is working on a 2D CT slice. In the second step, the lung lesion is segmented by the automatic region growing method in three-dimensional space with distance constraint and growing degree constraint. The distance constraint is used to define the largest growing distance and the growing degree constraint is used to restrict the voxels growing in each generation. By the multi-constraints, other lung tissues could be excluded on the original CT scans. Finally, in the lung lesion refining phase, a method based on lesion boundaries is provided to smooth abnormal regions around the lesion.

A. Original toboggan

The toboggan algorithm was first proposed for image contrast enhancement in [31]. On the gradient image, a sliding direction could be determined by searching the minimum

This article has been accepted for publication in a future issue of this journal, but has not been fully edited. Content may change prior to final publication. Citation information: DOI 10.1109/TMI.2015.2474119, IEEE Transactions on Medical Imaging

gradient magnitude of the neighborhoods of each pixel. Generally, the local minima pixels in the gradient image will be presented after repeating the search. Those pixels which "slide" to the same local minima will be labeled by the same mark. Thus, the gradient image could be segmented into a collection of small regions.

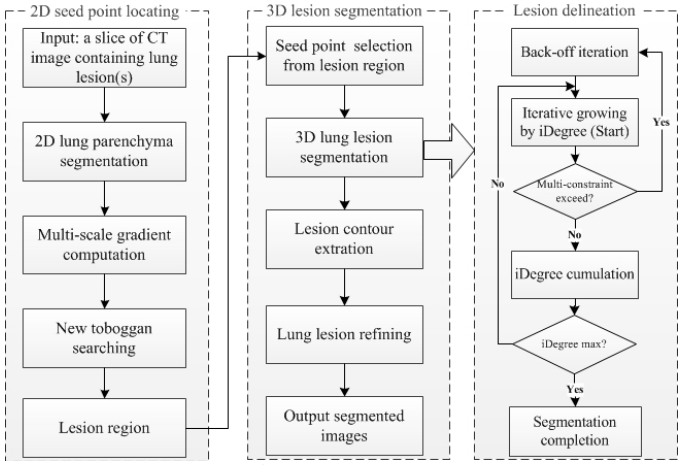

Fig. 2. Flowchart of the proposed segmentation algorithm

The original toboggan algorithm includes the following steps:

Step1. Calculate the gradient image.

Step2. Scan the four neighborhoods (or eight) of each pixel in the gradient image. As one slice is enough for the selection of the lesion seed point, the toboggan method in this paper is designed to segment the image into small regions in 2D view. The pixel would slide to its neighborhood with the minimum gradient value (if there is more than one pixel, the upper leftmost is obtained). The process will be repeated until it slides to the pixel with the local minimum. If the destination pixel is not labeled, a new label would be assigned to it.

Step3. Mark the pixels slide to the local minimum by the same label with the "minimum" pixel.

Step4. Repeat the process for all pixels. If a pixel is not labeled, its four neighborhoods (or eight) will be searched to find the local minimum. The process is repeated until all pixels in the image are segmented.

An overview of how the original toboggan approach works is shown in Fig 3. Where Fig. 3(b) is the small region circled by a black box in Fig. 3(a). The segmentation result with a sliding direction (triangular arrow flow) of each pixel using the original toboggan algorithm is presented in Fig. 3(b). Each small region circled by bold black lines will be marked by a unique label to further identify the targeting region. However, our improved toboggan algorithm can overcome some drawbacks of this conventional toboggan approach using a new algorithm for calculating the local minima, as shown in Fig. 3(c). The detailed explanation is presented in the next section.

Unlike the elongated pulmonary vessels, the morphologic characteristic of the lesion is closer to a regular circular one. Thus, according to the shape characteristic, four neighborhoods searching could reduce the probability of the lesion pixels sliding into the lung field. Therefore, the four neighborhoods are used to detect the toboggan gradient magnitude minima in this paper.

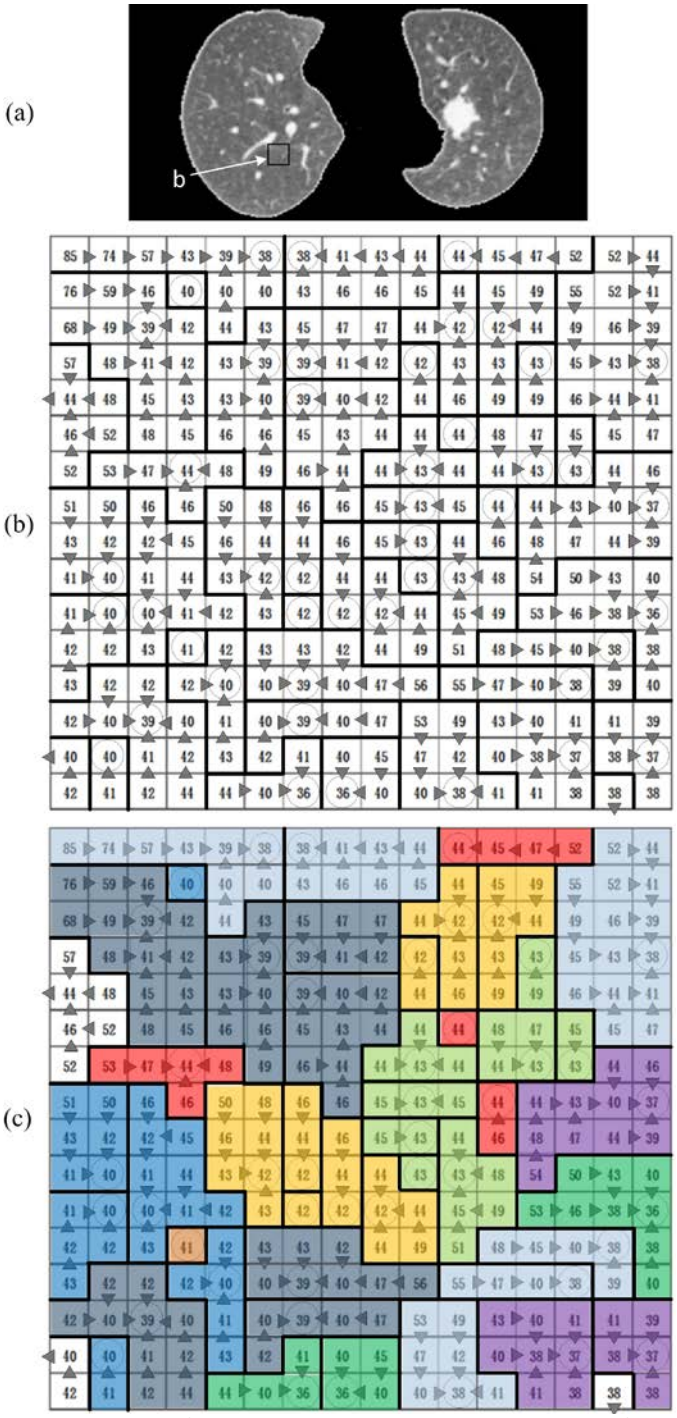

Fig. 3. A example of the toboggan method. (a) The gradient image of lung parenchyma. (b) The illustration of the working mechanism of the original toboggan method using the magnification of a partial lung parenchyma (the black box in (a)). Each number is the gradient magnitude of one pixel. Bold black lines define small regions sharing the same minima pixels. Triangular arrow flow shows the slide direction of each pixel. The local minima pixels are shown with circles. (c) The illustration of our improved toboggan method for finding the local minima pixels. Different from the original toboggan method, all small regions are categorized in the same color once their minima pixels have the same gradient magnitude, so that over segmentation can be effectively avoided.

B. Improved toboggan algorithm

Multi-scale Gaussian convolution could reflect image gradient changes in different directions. For example, different Gaussian convolution kernels could describe the gradient on

This article has been accepted for publication in a future issue of this journal, but has not been fully edited. Content may change prior to final publication. Citation information: DOI 10.1109/TMI.2015.2474119, IEEE Transactions on Medical Imaging

each coordinate axis (X-axis, Y-axis or Z-axis) in [37] and [38]. The multi-scale Gaussian gradient could also give a more accurate description for the lung image compared with other gradient computation methods. Besides, the highlighted noise would be eliminated by the improved toboggan algorithm after contrast enhancement using multi-scale Gaussian convolution. The first-order derivative of the multi-scale Gaussian kernel is used for lung gradient calculation in our paper.

$$N_{\sigma}\left(x,y\right)=exp\left(-\frac{x^{2}+y^{2}}{2\sigma^{2}}\right) \tag{1}$$

The kernel is a two-dimensional discrete convolution function with a standard deviation of σ. The multi-scale gradient magnitude is given by

$$G\left(x,y\right)=max\left[\sqrt{G_{\sigma}\left(x,y\right)}\right] \tag{2}$$

$G_{\sigma}\left(x,y\right)$ is a matrix of the gradient for pixels with the center $\left(x,y\right)$,where

$$G_{\sigma}=I_{(a,b)}\times\left[\left(\frac{\partial N_{\sigma}}{x}\right)^{2}+\left(\frac{\partial N_{\sigma}}{y}\right)^{2}\right] \tag{3}$$

$\left(a,b\right)$ denotes the coordinate of the pixel and $I_{(a,b)}$ is the intensity of pixel $\left(a,b\right)$ in the convolution kernel window. In this section, the gradient magnitude of all of the pixels is approximately [0,100] after multi-scale Gaussian convolution.

A gradient map of the lung parenchyma after the Gaussian convolution is presented in Fig. 4(a). The lesion has similar gradient magnitude with that of the vessels, fissures, bronchi, noise and other tissues. The original toboggan result is shown in Fig. 4(b), which produced serious over segmentation. Therefore, it cannot distinguish the lesion from the lung image. To overcome those challenges we present a toboggan gradient stack to calculate a new lung label image, which could exclude other tissues with a similar value to lesion on the gradient image. The toboggan gradient stack is used to store the local minima we searched for each pixel. The performance of the original and improved toboggan methods are compared through a simplified illustration in the Fig. 3(b) and (c). Instead of marking each small region with a unique label by the original method, small regions with the same minimum gradient value are marked as the same label, even when they are not morphologically connected, as shown in Fig 3(c). This approach can effectively minimize the over segmentation. The example of lung segmentation result using the improved toboggan method is shown in Fig. 4(c). The mathematical process is as following.

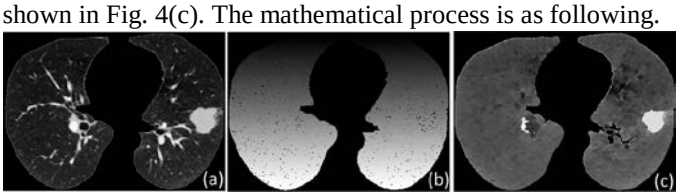

Fig. 4. The comparison of results by different toboggan methods. (a) shows a gradient image of lung parenchyma. (b) presents the over-segmentation by the traditional toboggan method. The lung parenchyma is divided into more than 1000 patches. (c) describes the result by the improved toboggan algorithm.

For the new toboggan, an empty stack is pre-defined to store the local minima gradient pixels. Each new local minimum gradient magnitude will be compared with all of the existing elements in the stack. A value in the stack with the maximum similarity to the new local minimum would be returned to mark the original source pixel. Otherwise the new minimum will be pushed into the stack and used to label the source pixel.

In the new toboggan algorithm, $L_{Source}\left(i,j\right)$ denotes the value of $\left(i,j\right)$ in the new label image of lung parenchyma. $G_{Source}\left(i,j\right)$ means the original gradient magnitude of $\left(i,j\right)$, where $SMax\left(ToboStack,G_{ToboMin}\left(i,j\right)\right)$ represents the function where we traverse the toboggan stack to find the maximum similar gradient magnitude. $ToboStack$ is the toboggan gradient stack and $G_{ToboMin}\left(i,j\right)$ means the minimum gradient value we searched for $\left(i,j\right)$ by its four-neighborhoods. The new label of $\left(i,j\right)$ is defined as:

$$\begin{aligned}L_{Source}\left(i,j\right)&=G_{Source}\left(i,j\right)*p+\\&\left[SMax\left(ToboStack,G_{ToboMin}\left(i,j\right)\right)\right]^{2}*q\end{aligned} \tag{4}$$

Here we choose the square of $SMax()$ to enhance the contrast between the lesion and lung field. For many lesions, the boundary points will disappear with the toboggan method as the boundaries are easily moved to their adjacent lung field. In order to achieve a more accurate lesion contour, these boundary points are kept by introducing p and q in the formula. p and q represent the weight of the two parts on the right side of the formula. In terms of a number of experiments on different lung field images, the optimal value of p is in the range of (0.0, 0.2] and q is [0.8, 1.0). Application of these two values can increase the weight of the original pixel gradient value and reduce the impact of noise. They are constrained with:

$$p+q=1 \tag{5}$$

The improved toboggan algorithm in this paper is as follows:

Algorithm 1 The improved toboggan algorithm

Input:
Gradient Image(GI); {The gradient magnitude of pixel p is GI(p).}
Stack GradientLabel(VG); {The gradient stack we pre-defined.}
Output:
Label Image(LI); {Result of toboggan}
Algorithm:
initialize VG; {The default value is NULL.}
bool IsMin; {IsMin is a flag to identify the toboggan process.}
for each p in GI {Pixels in the gradient image.}
IsMin = false;
Source = p;
while (!IsMin = true)
for each n∈N4(p)
IsMin = true;
if GI(n) < GI(P)
Change(Min)
IsMin = false;
end//if {IsMin is the true means where the minimum is found.}

This article has been accepted for publication in a future issue of this journal, but has not been fully edited. Content may change prior to final publication. Citation information: DOI 10.1109/TMI.2015.2474119, IEEE Transactions on Medical Imaging


```
    end//for
    if(IsMin = true)
      Bool IsExist = SMax(VG, Min);        {Try to match the min.}
      if (IsExist = true)
        Label(Source);     {Label the Source pixel by Eq. (4).}
        IsMin = true;
      end//if
      else
        VG.push_back(GI(p));     {Append the GI(p) to the VG.}
        Label(Source, Destination);   {Label the Source and Min.}
        IsMin = true;     {Reset flag.}
      end//else
    end//if
  end//while
end//for
```

By the improved toboggan method, the highlighted vessels, tracheal wall and other noise in the gradient image will be moved into the lung field while the lesion remains at a higher value. Therefore, the other tissues would be dimmed and the lesion could be enhanced in the label image for the subsequent automatic seed point selection. As shown in Fig. 5, a to l present solid nodules, and m to r denote ground-glass opacities. The first row in each image set shows the original gradient maps of these lungs, and the lesions are marked by yellow circles for clearer explanation. The second row describes new label images achieved by the novel improved toboggan algorithm. In Fig. 5h (1), multiple lesions in a lung parenchyma image are shown. They are successfully detected by the improved toboggan method and the seed region of two lesions is presented in Fig. 5h (2) and Fig. 5h (3). The two lesions will be segmented in accordance with the area of each lesion in the next section.

The new label images of the lung parenchyma after processing by the new toboggan method are shown in the second and fifth rows of Fig. 5. The lesions are apparently different from other tissues either in label value or in geometric appearance, such as area and morphology. Thereby, we set label value: 80, area: 60 pixels and diameter range: 3 to 30 mm as different thresholds for automatic extraction of lesion regions from the newly labeled images. The extracted lung lesion patches (Fig. 5, the third and sixth rows) are used for seed selection.

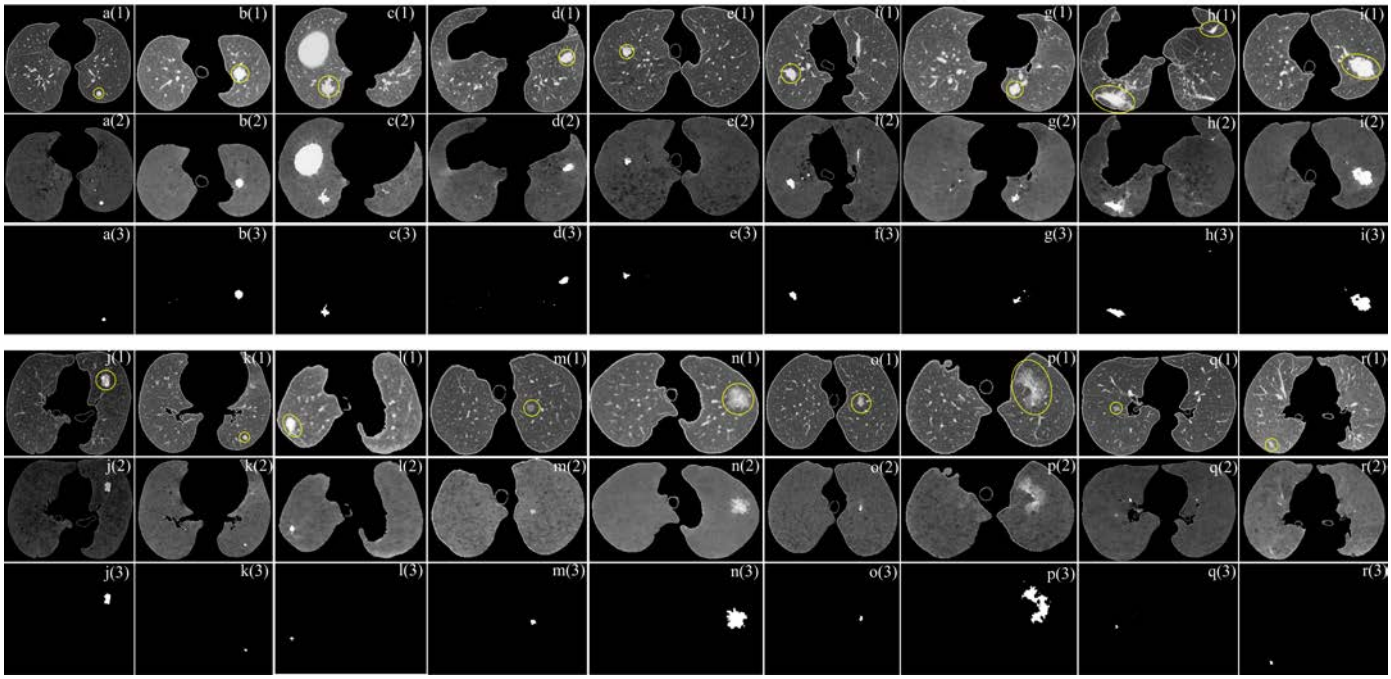

Fig. 5. Segmentation by the improved toboggan method, images a to l are solid nodules, and images m to r are ground-glass opacities (GGO). The first row in each image set shows the gradient maps and the second row presents the newly labeled images. The third one represents the images with lesion region patches. The highlighted parts denote the lesion regions for seed point selection and lung lesion segmentation.

C. Lesion segmentation with multi-constraints

In this section the proposed region growing algorithm with distance constraint and growing degree constraint for the lung lesion segmentation is described. A seed point is selected automatically in the lung lesion regions we obtained in section B. The multi-constraints are proposed to control the lesion segmentation. As the intensity of vessels and visceral pleura is close to that of the lung lesion, they are sometimes considered to be part of the adjacent lesions. These tissues are giant obstacles for lesion segmentation. In the next section of "Lung lesion refinement", a lung lesion refining method is used to get rid of the incorrect vascularized regions and other tissues.

In the process of lesion segmentation, a five-dimensional symbol vector is defined to describe the new lesion voxels in each generation (the meaning of the generation is same as that of the degree). The vector is organized by spatial coordinates, iDegree and iCount of each voxel. As the basic flag of growing segmentation, iDegree describes the generation number during segmentation. The initial seed point is the first generation, where the iDegree is given as 1. The twenty-six neighborhoods of the seed are detected and the voxels belonging to the lesion are the second generation, where iDegree is given as 2, and so on. Each lesion point will be assigned an iDegree in its five-dimensional symbol vector. iCount describes the total

This article has been accepted for publication in a future issue of this journal, but has not been fully edited. Content may change prior to final publication. Citation information: DOI 10.1109/TMI.2015.2474119, IEEE Transactions on Medical Imaging

number of lesion points increased in each generation. For example, in the first generation, iCount is given as 1 as there is only one lesion point (the seed point), while the range of iCount of the second generation is [0, 26]. A detailed description of the five-dimensional symbol vector during lesion segmentation is presented in Fig. 6. Each lesion point and its five-dimensional symbol vector are sequentially stored. For each point, an adaptive threshold could be obtained by traversing the voxels marked as a part of the nodule among its twenty-six neighborhoods. On the basis of the threshold, the other neighboring voxels will be determined whether they are marked as a part of the lesion. The next generation starts to grow once the segmentation of its previous generation finished. The maximum voxel count of iDegree in each generation is controlled by the iCount of its previous degree.

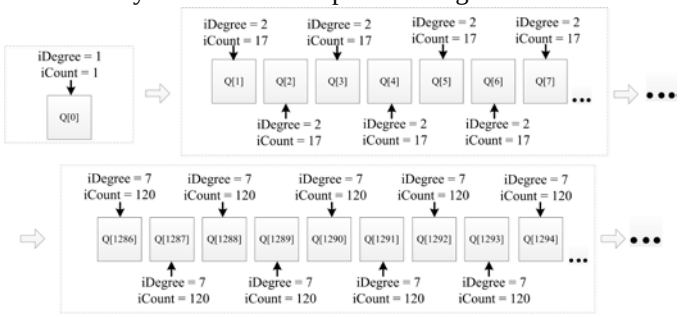

Fig. 6. A example of how the five-dimensional symbol vector works during lesion segmentation, where the spatial coordinate is hidden. iDegree denotes the generation of 3D growing, iCount presents the total number of this generation and Q[n] means the n-th voxel added to the lesion.

The "growing degree" constraint in this paper is used by calculating the difference between two adjacent generations. A "Back-off" mechanism will be triggered if the difference exceeds (better result could be obtained if the growing degree constraint is one of the value within: [iCount of previous degree]*[5, 10]). The "Back-off" will clear those voxels in the queue where their iDegree is included by the DegreeThreshold (DT), where normally the DT is one value in the scope of [3, 6]. The last voxel in the memory queue will be chosen as the seed point for the next more restricted generation growth.

The "Back-off" mechanism is described as follows:

Algorithm 2: the growing "back-off" algorithm

```
If((CurrentNode - FrontNode)>Threshold){Node is the generation}
  CurrentDegree = NodulePoints[last]. iDegree
 for each i in NodulePoints      { Traverse the nodule point queue.}
  SeedPoint = NodulePoints[i];
  if(SeedPoint. iDegree - CurrentDegree <DegreeThreshold)
     NodulePointsMark[SeedPoint] = NULL;      {Clear the point.}
  end //if
  if(SeedPoint. iDegree - CurrentDegree =DegreeThreshold)
       SeedQueue.push_back(SeedPoint);      {Get the new seed.}
  end //if
 end //for
BackIteration(SeedQueue); {Next generation: iterative 3D growing.}
```

On the basis of the area of the lung lesion we have obtained by the improved toboggan algorithm in Section II-B, a largest distance constraint (LDC) is defined to restrict the growth in each direction during lesion segmentation. Its morphologic meaning is the maximum Euclidean distance between the center point and lesion boundary points. The LDC we use is calculated as follows:

$$LDC = \sqrt{Area / \mathrm{PI}} * \mathrm{Range} \tag{6}$$

where $Area$ is the size of the lung lesion region obtained by the improved toboggan algorithm in Section II-B. For small lesions, (diameter of the lesion is approximately 3mm, or the number of lesion pixels in a CT slice with the largest lesion area is less than 60) better result could be obtained when the Range is controlled between 0.5 to 1, and for the large lesions it is 5 to 10.

Two-norms of each lesion voxel is used to judge whether it exceeds the LDC limit. A decision mechanism of voxel p based on the two-norms is described as follows:

$$Diff = \left\| p - S \right\|_2 \tag{7}$$

where $\left\| p - S \right\|_2$ means the Euclidean distance from p to the initial seed point; here we use S to describe the seed point. Then, a comparison between $Diff$ and LDC is implemented:

$$K = Diff - LDC \tag{8}$$

If K is non-negative, it means p exceeds the largest growing distance limit. Then, we need the voxel intensity of p to determine whether the growth of this direction should be continued. A straight line constituted by S and the current voxel point p is determined as:

$$l = ax + by + cz + d \tag{9}$$

The slope of l is calculated by the two coordinates $p_{(x,y,z)}$ and $S_{(x,y,z)}$. We use the seed S as the starting point to traverse all lesion voxels in the direction determined by l. The mean intensity is calculated as:

$$mean = \sum_{i=1}^{N} p_i / N \tag{10}$$

where N is the total lesion voxel number of l from S to p (p is excluded) and p_i is the voxel intensity of the voxels of l. If the intensity of p is significantly lower or higher than the $mean$, it indicates that point p belongs to the lung field or other organs but not the lesion. The segmentation in this direction will be stopped. If the LDC is too small, however, the segmentation could not obtain the entire lesion (such as the cavities), so a fine distance constraint could not only inhibit the disturbance of the vascularized regions and other highlighted tissues close to the lesion boundaries in CT scans, but also ensure a good tumor profile.

D. Lung lesion refinement

In this section, a lung lesion refining method is used for more accurate lesion boundary definition. Since the iterative growing segmentation only uses grayscale information but neglects the morphologic characteristics of the lesion, miniscule incorrect segmentation exists after Section C. In the two adjacent lesion slices, for example, one slice includes a slender vessel but its

This article has been accepted for publication in a future issue of this journal, but has not been fully edited. Content may change prior to final publication. Citation information: DOI 10.1109/TMI.2015.2474119, IEEE Transactions on Medical Imaging

adjacent slice does not. It is displayed as a mutation on the original transverse images. In this section, those mutations will be smoothed for accuracy improvement. Here we use the lesion boundaries in each slice. The refining method in this paper only works on the adjacent lesion slices in a cross-section view, so the two slices being processed are regarded as the center slice CI and its adjacent slice is CI' (the larger profile is defined as CI' in this paper). The direction from the neck to the abdomen is considered as the main direction. The steps of the lung lesion refining method are described as follows:

Step1. Calculate the center of the gravity (COG, or a center point in the lesion) in CI:

$$COG = \sum_{i=1}^{M} CI_i / M \tag{11}$$

where M denotes the number of lesion pixels in CI, and CI_i represents the coordinate of the lesion points.

Step2. Extract the lesion contour of CI and CI';

Step3. Compute the distance between COG and the boundary point b_i on CI:

$$Dis(b_i) = \left\| b_i - COG \right\|_2, i = (0,1...n) \tag{12}$$

where $\left\| b_i - COG \right\|_2$ means the two-norms of (b_i, COG), and n is the total number of boundary points. $Dis(b_i)$ represents the Euclidean distance from b_i to COG.

Step4. Calculate the distance between COG and the boundary point b_i' on CI'. Draw the straight line which is determined by COG to b_i'. $Dis(b_i')$ is used to describe the distance:

$$Dis(b_i') = \left\| b_i' - COG \right\|_2, i = (0,1...n') \tag{13}$$

where n' represents the boundary points in CI'. On the original transverse images, voxels b_i and b_i' are the boundary points of lesion. We will process each difference between $Dis(b_i')$ and $Dis(b_i)$ in the same direction in the next steps.

Step5. Execute Step 4 on all boundary points in CI'. $Dis(b_i')$ and $Dis(b_i)$ in each direction are stored for the subsequent calculation in Step 6.

Step6. Obtain the average distance Avg:

$$Avg = \sum_{points} \left(\left\| Dis(b_i') - Dis(b_i) \right\| \right) / points \tag{14}$$

where $points$ represents the number of b_i' we should process. For each boundary point b_i' if the distance $Dis(b_i')$ is larger than Avg (in some complex structure of lesions, the larger one is $Dis(b_i)$, but here we use $Dis(b_i')$ to represent it), it is modified with the following equation:

$$NewDis(b_i') = Dis(b_i') - (Dis(b_i') - Avg) * p \tag{15}$$

where p represents the weight of points larger than Avg, $NewDis(b_i')$ is the new location of b_i' after refining (if the larger one is $Dis(b_i)$, the $Dis(b_i')$ in Eq. (15) should be replaced by $Dis(b_i)$ and the result is $NewDis(b_i)$). Fig. 7 is a simple example of how lung lesion refining works.

A more accurate lesion boundary could be detected using our method with accurate lung parenchyma edges for some special solid nodules, such as juxta-pleural, where a significant portion of the nodule is connected to the pleural surface, chest wall or mediastinum (Fig. 8(a)). TBGA alone can offer a reasonable good segmentation in such a case, but part of the lesion attached tissues in the junction area might be considered as a part of the lung lesion (Fig. 8(d)). To avoid that, the contour of the lung parenchyma is introduced to constrain the TBGA. However, this approach causes a concave rather than a convex surface of the lesion (Fig. 8(e)), which is against the common morphology of a lung lesion [39]. Therefore, we further constrain the curvature of the lesion to ensure the convexity (Fig. 8(f)).

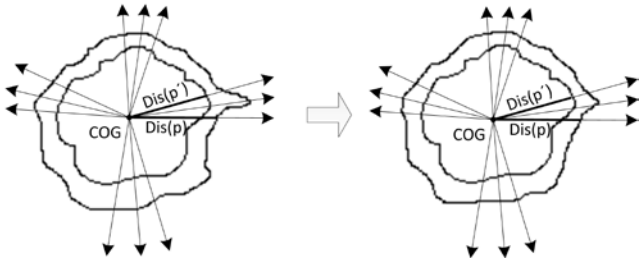

Fig. 7. Example of lung lesion refining, where the internal profile represents the center image, and the external one represents the adjacent slice. (a) presents two contours before boundary smoothing, (b) denotes the contours after boundary refining.

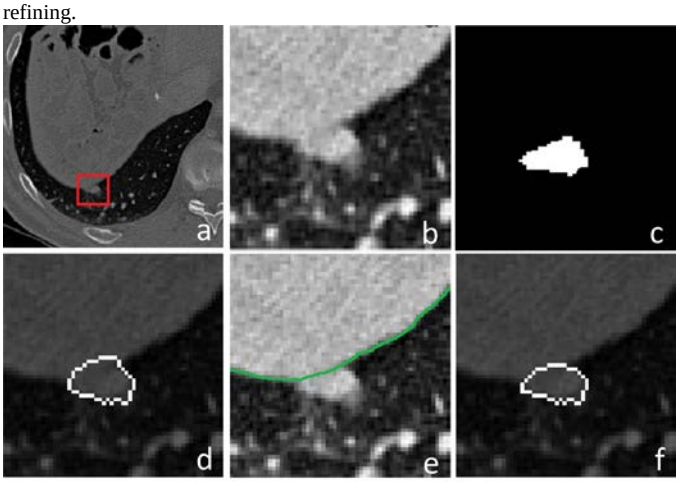

Fig. 8. Lung lesion segmentation for the juxta-pleural lesion, (a) is the original image and the nodule has been enclosed in a red box. (b) is the magnified lesion image. (c) denotes the lesion region after the improved toboggan method. (d) is the segmentation result of TBGA without the restriction of lung outline. The lung boundary in (e) has been marked by a green line. And (f) is the final segmentation result of TBGA with the restriction of the lung border.

III. Results

A. Dataset

Both publicly available and in-house acquired datasets were used to evaluate the performance of our TBGA method. Here,

This article has been accepted for publication in a future issue of this journal, but has not been fully edited. Content may change prior to final publication. Citation information: DOI 10.1109/TMI.2015.2474119, IEEE Transactions on Medical Imaging

850 lung lesions from the LIDC-IDRI database were used. The slice thicknesses for those images ranged from 1.25 to 2.50 mm with a 0.70 mm × 0.70 mm resolution. Those lesions consisted of 757 solid nodules, 52 ground-glass opacities and 41 air-containing cavity tumors, which are taken as a separate category since their morphology is completely different from that of a solid nodule and GGO. Their diameter ranged from 3 mm to 30 mm (average 9.80 mm). Each lesion was manually segmented by four readers on average and we used the average manual segmentation results from the LIDC-IDRI database as the standard [11].

The clinical dataset we used consisted of 100 NSCLC patients with 121 lesions in total since 21 out of 100 patients contained two lesions. The standard-of-care clinical CT scans have a high resolution with contrast enhancement and their slice thicknesses varied from 0.50 to 1.00 mm. About 80 solid nodules, 28 ground-glass opacities and 13 air-containing cavities were contained and all of the solitary, juxta-pleural and juxta-vascular lesions were included.

B. *Evaluation metrics*

Dice Coefficient (DC) [40] is used to measure the lesion segmentation accuracy:

$$DC_{A,G} = \left(2\left|A \cap G\right| / \left(\left|A\right| + \left|G\right|\right)\right) * 100\% \qquad (16)$$

in which A and G are two clustered lesion volumes (e.g., manual or automatic) respectively. $DC_{A,G}$ represents the DC of A and G.

Besides, Hausdorff Distance (HD) ([41] and [42]) is also used as a similarity measure for segmentation evaluation as shown in Eq. (17):

$$HD_{A,G} = \max_{a \in A}\left(d\left(a,G\right)\right),\ d\left(a,G\right) = \min_{g \in G}\left\|a - g\right\| \qquad (17)$$

where $d\left(a,G\right)$ denotes the distance from A to G.

To demonstrate the accuracy of the new algorithm, we tested the segmentation of different types of pathological lungs as discussed in the introduction using the level set method (LS) provided by Li [43] and the skeleton graph cut algorithm (SGC) [44] by 3D Med [45]. In this paper, both DC and HD are used to evaluate LS, SGC and TBGA. We used the results provided by the two radiologists with more than ten years of experience in clinical diagnosis as the segmentation standard for the in-house dataset evaluation. They are mainly responsible for manual segmentation. The manual results from the two radiologists are marked as R1 and R2 respectively. The result from our automatic algorithm is denoted as TBGA. Besides, radiologist 1 also provided the manual seed point as the input of lesion segmentation using our growing method in this study and the result is denoted as MBGA. In MBGA, one human interaction is required. MBGA is used to prove that the auto segmentation is stable and the automatic seed point is effective.

C. *Overall performance*

We tested 850 lesions from the LIDC-IDRI database using the new algorithm and correctly identified 819 lesions with 73 wrong detection results. Besides, 115 successful segmentation and 15 incorrect results were obtained from the 121 in-house clinical lesions. The true positives of detection on the two datasets were 96.4% and 95.0% respectively. Table I shows the detailed results of detection and segmentation on all lesions.

TABLE I
A LIST OF DETECTION SENSITIVITY FOR TWO DATASETS: THREE TYPES OF LESIONS ARE CONSIDERED. FOR EACH TYPE, THE NUMBER OF TESTED CASES, CORRECTLY/INCORRECTLY IDENTIFIED (IN PARENTHESES) CASES ARE COUNTED. TRUE POSITIVES AND FALSE POSITIVES OF THE TWO DATASETS IN TOTAL ARE GIVEN IN THE LAST COLUMN. DUE TO THE PULMONARY MASS WHICH IS CONSIDERED AS LESION IS THE ONLY FOCUS IN THIS STUFY, HERE THE TRUE POSITIVE IS DEFINED AS THE NUMBER OF CORRECTLY LOCATED LESIONS/THE TOTAL NUMBER OF MANUALLY LOCATED LESIONS. THE FALSE POSITIVE IS DEFINED AS THE NUMBER OF INCORRECTLY LOCATED LESIONS/THE TOTAL NUMBER OF MANUALLY LOCATED LESIONS.

Results	LIDC-IDRI data	In-house data	TP/FP
Solid nodule	757(729/67)	80(75/12)	96.1%/9.0%
GGO	52(52/0)	28(27/2)	98.8%/2.5%
Cavity	41(38/6)	13(13/1)	94.5%/12.9%
Total	850(819/73)	121(115/15)	96.2%/9.1%

D. *Experiments on the LIDC-IDRI dataset*

Fig. 9 shows the comparison of the segmentation results by three methods (TBGA vs. manual, LS vs. manual and SGC vs. manual) using DC on different lesion types (all lesions, solid nodules, ground-glass opacities and cavities) from the LIDC-IDRI database.

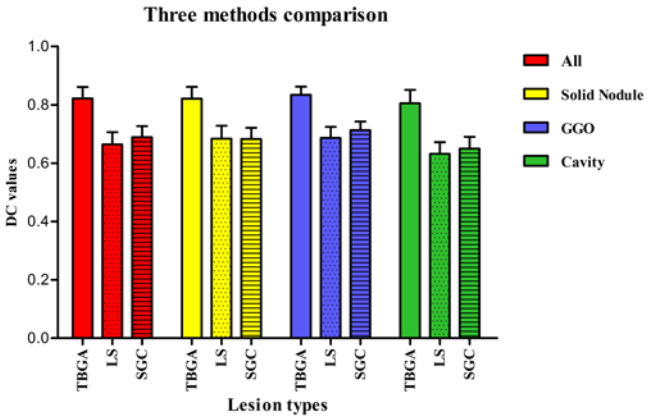

Fig. 9. The DC values of TBGA vs. manual, LS vs. manual and SGC vs. manual of all lesions including solid nodules, ground-glass opacities and cavities from the LIDC-IDRI database.

In Fig. 9, the DC value of TBGA vs. manual segmentation on all lesions from the LIDC-IDRI dataset is 81.57% on average with a standard deviation of 3.90%. The segmentation accuracy by the DC increased 15.33% and 11.67% compared with LS (66.24%, 4.20%) and SGC (69.90%, 3.20%).

All of the improvement of segmentation accuracy on solid nodules, ground-glass opacities and cavity tumors is higher than 12% when comparing the DC values of TBGA vs. manual with those of LS vs. manual. Furthermore, the segmentation accuracy improvement of DC on solid nodules, ground-glass opacities and cavity tumors is higher than 10% when comparing the DC values of TBGA vs. manual with those of SGC vs. manual. Table II represents all statistical results of the three segmentation methods on cases from the LIDC-IDRI database.

The interior of air-containing tumors (cavities) tends to be black and the periphery is highlighted in CT scans. The cavity

This article has been accepted for publication in a future issue of this journal, but has not been fully edited. Content may change prior to final publication. Citation information: DOI 10.1109/TMI.2015.2474119, IEEE Transactions on Medical Imaging

is more likely to be a malignant tumor. If such a lesion occurs at the center of the lung parenchyma, it is often accompanied by a lot of burrs as shown in Fig. 10(a). After the new toboggan method, the cavity region is highlighted in Fig. 10(b) and the lesion region for seed point selection is shown in Fig. 10(c).

Since the morphological specificity of the cavity, the segmentation needs to include both the internal hole and the external cavity wall. However, the surrounding burr is a large obstacle for manual segmentation as tedious manual drawing sometimes could not recognize the surrounding burrs as shown in Fig. 11. The image set (a) represents the segmentation results by TGBA and (b) describes the LIDC-IDRI manual delineation.

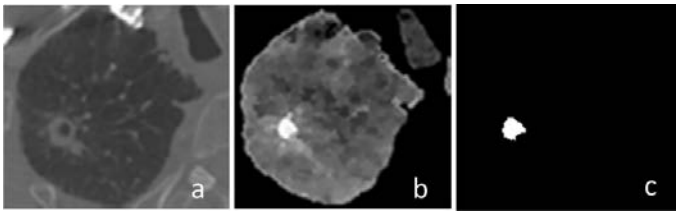

Fig. 10. The toboggan results for a cavity tumor. (a) describes the original lesion slice. (b) is the improved toboggan search result and (c) represents the lesion region of the cavity tumor.

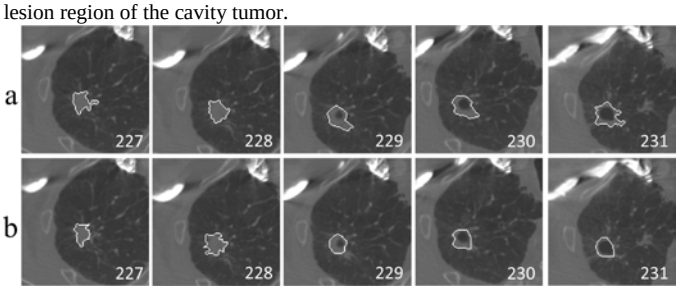

Fig. 11. The segmentation results of the cavity tumor. (a) represents the TBGA segmentation and (b) denotes the manual delineation results provided by the LIDC-IDRI database.

TABLE II

THE COMPARISON AMONG TBGA, LS AND SGC IN THE CATEGORY OF ACCURACY ASSESSMENT IN DIFFERENT LESION TYPES, RUNTIME COST, AND THE NUMBER OF HUMAN INTERACTIONS. THE DC VALUES ARE EXPRESSED AS MEAN ± STANDARD DEVIATION.

Method	TBGA	LS	SGC
Solid nodule (DC)	81.56%±4.00%	68.95%±3.70%	69.52%±2.90%
GGO (DC)	82.72%±2.70%	68.58%±3.80%	72.59%±2.80%
Cavity (DC)	79.93%±4.50%	62.07%±4.90%	65.03%±4.10%
ALL (DC)	81.57%±3.90%	66.24%±4.20%	69.90%±3.20%
ALL (HD)	3.52	6.17	5.50
Runtime	7.20s	60.02min	50.21s
Interaction	0	1	3

E. Experiments on the clinical dataset

Detailed segmentation results of lung lesions on the clinical dataset are described in Fig.13. Table III and Table IV present the cross comparisons of lesion segmentation results between the two radiologists, TBGA, LS and SGC in DC and HD on the clinical dataset, respectively. P1 to P13 are solid nodules and P14 to P19 are ground-glass opacities, which were all randomly selected. The comparison reveals that as the gold standard, the DC and HD of the two radiologists are 81.61% and 3.89. TBGA is the only method that is able to provide the competitive performance with the gold standard ($P > 0.05$ in both DC and HD). The differences in DC between manual segmentations and LS are statistically significant ($P < 0.001$), which indicates 13.85% and 14.84% improvement using TBGA. Similarly, comparing with SGC, TBGA offers 9.18% and 10.37% accuracy improvement in DC. The differences in HD between manual and LS as well as between manual and SGC are also significant ($P < 0.05$). For LS or SGC, the differences with manual by HD are all larger than 5.40, whereas the differences of using TBGA are smaller than 3.60.

F. Human interaction

The number of human interaction of TBGA, LS and SGC are described in Table II. The segmentation method marked as SCES (single click ensemble segmentation) [16] requires one interaction for an initial growing seed point. The number of human interactions in SGC is 3, including the selection of the foreground/background points and a threshold for pre-segmentation. LS needs an optimal initial seed point for iterations so its human interaction is 1 on average. Compared with SCES, LS and SGC, our algorithm (TBGA = 0) got a significant advantage with the automatic mechanism.

G. Sensitivity of segmentation

The lesion region we obtained in Section II-B is the premise of the segmentation method we proposed in Section II-C. Since the lesion region is used as a reference of multi-constraints, the slice with the largest lesion area in those lesion slices is preferred. The upper and lower thresholds are always critical for segmentation methods based on region growing. For different types of lesions, the threshold should be different. Fig. 12(a) denotes the manual segmentation results and Fig. 12(b) shows the segmentation results with the threshold of $Mean \pm 100$ HU (Hounsfield unit) for the twenty-six neighborhoods judgment of each voxel during the region growing process. And $Mean$ is the adaptive threshold of each voxel during the 3D growing. Fig. 12(c) presents the results with $Mean \pm 200$ HU. We can find that different thresholds play a major role in segmentation. Normally, we choose the threshold of [-200, 300] HU at the $Mean$ as the criteria for lesion growing. For GGO, the lesion intensity should be controlled in the range of [400, 700] HU. This upper threshold of GGO coincides with the minimum solid nodule intensity value (the intensity range of the solid nodule is [700, 2000] HU). Thus, the intensity of the seed point to distinguish between a solid nodule and other lesions in this method is about 700 HU.

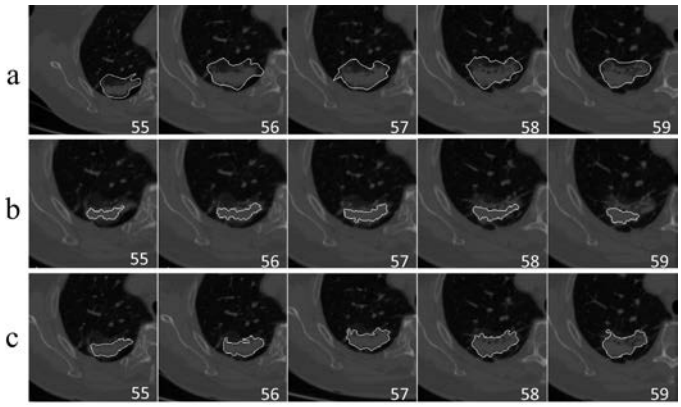

Fig. 12. Segmentation results with different thresholds. (a) denotes the manual segmentation results, (b) describes the results with the threshold of $Mean \pm 100$ HU and (c) includes the results with a $Mean \pm 200$ HU.

This article has been accepted for publication in a future issue of this journal, but has not been fully edited. Content may change prior to final publication. Citation information: DOI 10.1109/TMI.2015.2474119, IEEE Transactions on Medical Imaging

TABLE III
THE SEGMENTATION COMPARISON BY DC, THE PERCENTAGE PRESENTED DENOTES THE PROPORTION OF VOXELS IN AGREEMENT. R1 = RADIOLOGIST 1, R2 = RADIOLOGIST 2, TBGA = TOBOGGAN BASED GROWING AUTOMATICALLY, LS = LEVEL SET, SGC = SKELETON GRAPH CUT.

Data	DC value % R1 vs. R2	DC value % R1 vs. TBGA	DC value % R2 vs. TBGA	DC value % TBGA vs. LS	DC value % R1 vs. LS	DC value % R2 vs. LS	DC value % TBGA vs. SGC	DC value % R1 vs. SGC	DC value % R2 vs. SGC	DC value % LS vs. SGC
P1	83.40	82.87	84.22	79.57	63.26	70.61	85.29	78.09	75.90	81.91
P2	77.59	82.52	80.74	76.39	69.58	62.47	77.83	73.54	75.24	77.07
P3	72.85	73.88	65.32	61.78	60.49	63.10	65.46	71.18	66.67	69.36
P4	80.96	78.38	73.25	77.69	65.13	62.18	69.71	67.20	67.82	68.60
P5	84.22	85.05	86.17	80.41	69.64	66.92	71.48	69.54	54.26	63.72
P6	92.47	79.40	79.62	77.25	68.57	60.46	72.78	73.38	75.98	71.53
P7	78.35	75.95	80.93	72.63	60.93	66.34	70.94	68.16	73.53	64.58
P8	82.60	77.17	79.55	80.12	62.41	68.55	71.34	73.34	75.04	72.98
P9	90.25	72.69	77.41	74.98	65.67	72.03	70.22	74.89	69.97	71.53
P10	78.20	88.13	87.92	82.04	70.13	74.21	81.25	75.23	78.57	79.15
P11	82.56	76.69	80.94	71.23	65.44	68.60	73.89	71.01	68.22	53.94
P12	90.48	75.89	82.67	80.51	65.95	67.29	70.77	66.82	72.01	75.29
P13	82.92	77.72	88.80	76.35	64.19	65.13	73.15	70.19	75.78	75.83
P14	72.16	75.12	79.12	70.46	69.52	68.31	66.54	67.28	68.23	78.65
P15	81.50	85.77	83.29	72.70	60.37	66.25	68.46	65.64	65.78	74.55
P16	85.20	85.14	67.93	53.38	69.97	63.41	63.75	70.48	72.24	76.12
P17	77.63	76.82	85.27	70.52	67.29	60.66	67.12	64.93	62.64	76.15
P18	74.22	80.13	83.40	72.73	61.95	58.49	68.90	66.24	69.23	79.70
P19	82.95	79.98	88.18	65.24	65.58	67.62	66.64	67.62	70.55	74.23
Ave	81.61	79.43	80.77	73.47	65.58	65.93	71.34	70.25	70.40	72.89
p-value	-	0.195	0.673	<0.0005	<0.0001	<0.0001	<0.0001	<0.0001	<0.0001	<0.0002

TABLE IV
THE SEGMENTATION COMPARISON BY HD, R1 = RADIOLOGIST 1, R2 = RADIOLOGIST 2, TBGA = TOBOGGAN BASED GROWING AUTOMATICALLY, LS = LEVEL SET, SGC = SKELETON GRAPH CUT.

Data	HD value R1 vs. R2	HD value R1 vs. TBGA	HD value R2 vs. TBGA	HD value TBGA vs. LS	HD value R1 vs. LS	HD value R2 vs. LS	HD value TBGA vs. SGC	HD value R1 vs. SGC	HD value R2 vs. SGC	HD value LS vs. SGC
P1	2.05	1.66	2.79	4.72	3.98	3.96	3.82	2.02	1.76	1.16
P2	2.41	2.22	3.18	5.56	4.67	4.85	6.46	4.51	5.14	6.45
P3	8.77	5.33	3.70	4.40	3.91	4.45	6.91	3.63	5.86	6.37
P4	3.65	4.49	3.85	6.32	7.76	4.12	7.37	4.46	5.49	6.28
P5	4.80	3.93	1.62	9.95	5.34	9.55	9.81	6.89	9.70	7.52
P6	1.19	2.70	2.54	6.64	6.94	3.96	5.06	6.91	3.42	7.63
P7	5.08	3.12	6.46	8.85	4.12	7.36	7.04	5.25	5.26	5.99
P8	6.12	5.30	4.21	6.71	3.85	7.79	4.87	3.76	4.79	4.01
P9	1.83	3.42	1.76	4.06	7.46	5.92	6.56	2.76	3.70	3.15
P10	3.77	2.01	4.97	5.06	9.21	6.73	8.19	5.19	4.87	9.59
P11	5.94	4.56	3.21	7.47	12.85	8.54	10.71	10.73	8.45	9.81
P12	3.20	3.00	2.27	7.56	5.37	6.40	2.79	6.91	7.59	5.63
P13	1.68	1.32	2.49	4.35	1.45	4.11	6.83	3.48	1.30	2.45
P14	3.00	2.83	3.60	6.85	4.71	5.25	2.46	4.83	3.45	5.16
P15	8.12	9.38	6.52	7.41	10.75	9.65	7.34	8.16	8.12	10.58
P16	3.57	4.51	3.18	8.59	3.64	2.43	10.85	6.94	4.65	6.94
P17	2.06	2.48	3.29	10.21	6.26	8.45	3.16	8.72	9.91	8.72
P18	1.74	2.00	3.83	4.05	5.21	6.25	4.71	9.16	5.33	7.08
P19	4.97	3.75	2.02	5.38	8.14	4.61	1.45	2.86	4.20	5.71
Ave	3.89	3.57	3.45	6.53	6.09	6.02	6.13	5.64	5.42	6.33
p-value	-	0.636	0.457	<0.0004	0.010	0.004	0.008	0.025	0.048	0.003

TABLE V
THE COMPUTATION TIME FOR 19 PATIENTS, TBGA = TOBOGGAN BASED GROWING AUTOMATICALLY, LS = LEVEL SET, SGC = SKELETON GRAPH CUT.

Data	Lesion Slice Info	TBGA (s)	LS (min)	SGC (s)
P1	512×512×12(1 mm)	4.72	15.00	25.30
P2	512×512×29(1 mm)	9.55	93.80	66.70
P3	512×512×31(1 mm)	7.83	68.20	58.40
P4	512×512×19(1 mm)	5.36	41.80	45.90
P5	512×512×12(1 mm)	3.79	26.40	23.70
P6	512×512×74(1 mm)	16.29	162.80	120.50
P7	512×512×13(1 mm)	6.09	19.50	22.60
P8	512×512×15(1 mm)	4.50	48.00	28.90
P9	512×512×75(0.5 mm)	23.67	240.00	95.20
P10	512×512×37(1 mm)	10.83	55.50	39.30
P11	512×512×18(1 mm)	5.92	37.80	29.80
P12	512×512×41(1 mm)	10.24	25.20	56.70
P13	512×512×15(1 mm)	6.80	22.50	26.30
P14	512×512×12(1 mm)	3.87	18.00	18.60
P15	512×512×34(1 mm)	7.61	71.40	34.90
P16	512×512×14(0.5 mm)	2.16	21.00	19.50
P17	512×512×26(1 mm)	8.38	83.20	38.10
P18	512×512×11(1 mm)	5.01	35.20	15.40
P19	512×512×9(1 mm)	4.85	28.80	10.60
Ave	-	7.76	58.63	43.86

H. Computing time

In addition, the time efficiency of our TBGA method is greatly improved compared with LS and SGC. Table V shows the detailed lesion slice information of the 19 patients above and their time consumption. All of the three methods are tested under the same condition. For the multi-slice helical clinical CT images, compared with LS and SGC, our algorithm could provide a much faster response (from P9, 75 slices with 23.67s to P5, 12 slices with only 3.79s). P9 is an exception among those lesions as it contains two lesions, one is the 95th slice to the 143rd slice and the other is the 485th slice to the 510th slice, which leads to double executions so its time consumption is the longest.

I. Repeatability and Stability

In addition, radiologist 1 provided one manual seed input for each lesion instead of the automatic seed point selection by

This article has been accepted for publication in a future issue of this journal, but has not been fully edited. Content may change prior to final publication. Citation information: DOI 10.1109/TMI.2015.2474119, IEEE Transactions on Medical Imaging

TBGA for the in-house clinical dataset to certify the effectiveness of our automatic seed point. The result is denoted as the manual seed and growing automatically (MBGA). One human interaction is required in MBGA and the 3D growing segmentation method of MBGA is same with that of TBGA. We also used DC to evaluate the similarity of MBGA when compared with TBGA, as shown in Fig. 13. The average DC value for TBGA vs. MBGA is 93.59% on 115 cases.

In Fig. 13, the front 75 lesions are solid nodules, the following 13 are air-containing cavity tumors and the rear 27 lesions are ground-glass opacities. All of the DC values in Fig.13 for each lesion are the average of the test-retest. The black block represents the DC value of R1 vs. TGBA and the blue denotes that of R1 vs. MBGA. The segmentation accuracy of some lesions could reach more than 90%. However, the accuracy on a few lesions is lower than 60%. The DC values of R1 vs. TBGA and those of R1 vs. MBGA are similar for each lesion, and most of them are in the range of 75% to 85% in total.

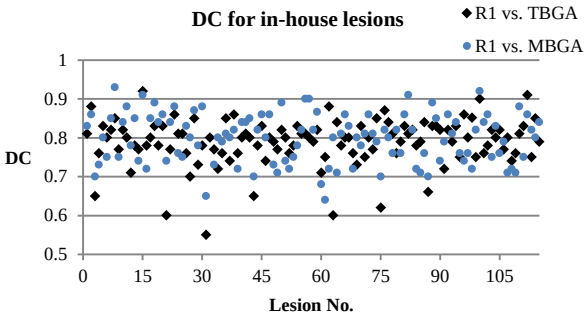

Fig. 13. The DC values on the 115 in-house lesions by R1 vs. TBGA and R1 vs. MBGA.

The segmentation results by our algorithm, R1, R2, LS and SGC are shown in Fig.14 through Fig.16 (solid nodules) and Fig.17 through Fig.19 (ground-glass opacities). The pixel intensity of the solitary GGO in Fig. 17 is similar to that of the lung field. A significant portion of the juxta-pleural GGO in Fig. 18 is connected to the pleural surface and the juxta-vascular GGO in Fig. 19 has significant connection to the neighboring vessel. The above three ground-glass opacities are the representatives of the three lesion types (solitary, juxta-pleural, juxta-vascular). Following, six segmentation results (both solid nodules and ground-glass opacities) in 3D view are represented in Fig.20.

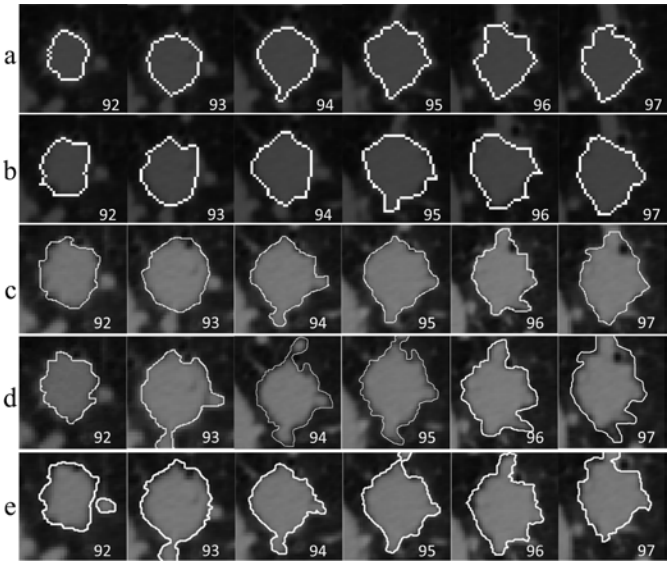

Fig. 14. Segmentation results of solid nodules. (P2, slices 92nd–97th); (a) TBGA, (b) R1, (c) R2, (d) LS, (e) SGC.

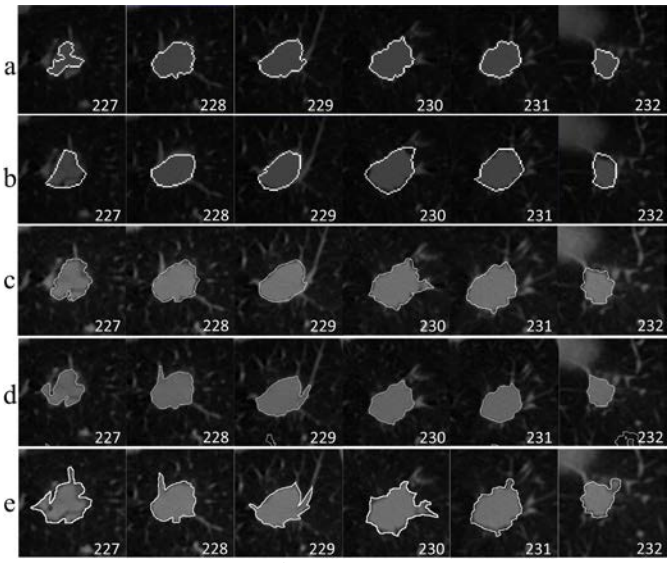

Fig. 15. Segmentation results of solid nodules. (P4, slices 227th–232nd); (a) TBGA, (b) R1, (c) R2, (d) LS, (e) SGC.

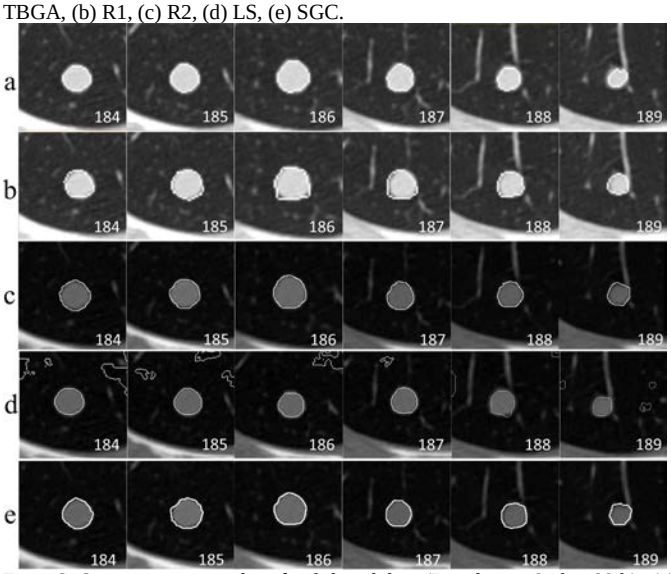

Fig. 16. Segmentation results of solid nodules. (P1, slices 184th–189th); (a) TBGA, (b) R1, (c) R2, (d) LS, (e) SGC.

This article has been accepted for publication in a future issue of this journal, but has not been fully edited. Content may change prior to final publication. Citation information: DOI 10.1109/TMI.2015.2474119, IEEE Transactions on Medical Imaging

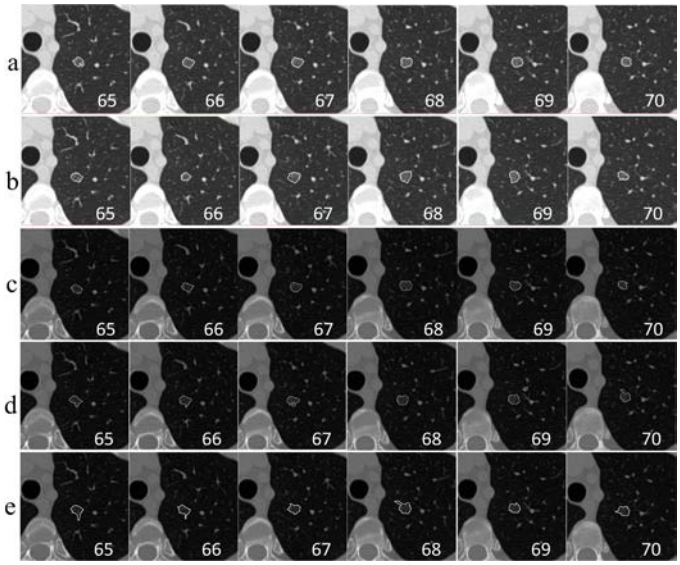

Fig. 17. Representative segmentation results of the solitary GGO. (P14, slices 65th–70th); (a) TBGA, (b) R1, (c) R2, (d) LS, (e) SGC.

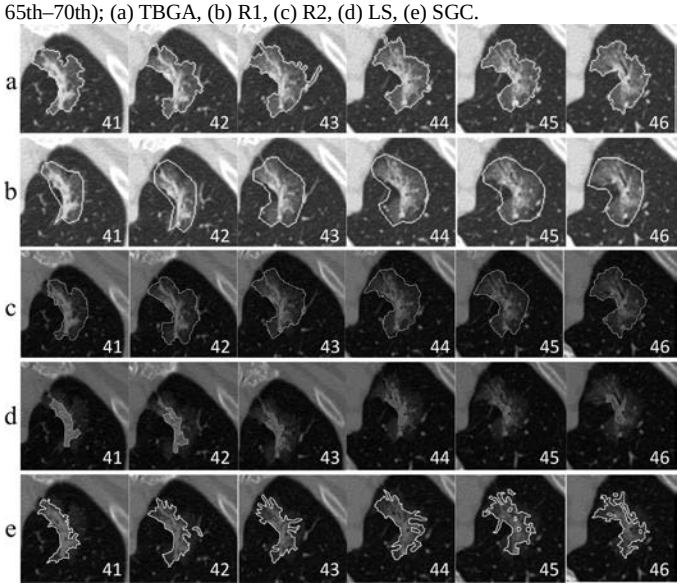

Fig. 18. Representative segmentation results of the juxta-pleural GGO. (P17, slices 41st–46th); (a) TBGA, (b) R1, (c) R2, (d) LS, (e) SGC.

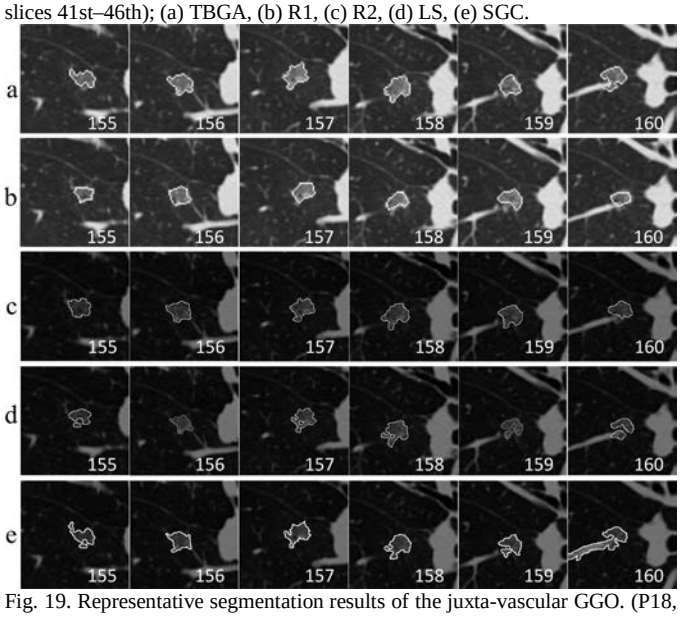

Fig. 19. Representative segmentation results of the juxta-vascular GGO. (P18, slices 155th–160th); (a) TBGA, (b) R1, (c) R2, (d) LS, (e) SGC.

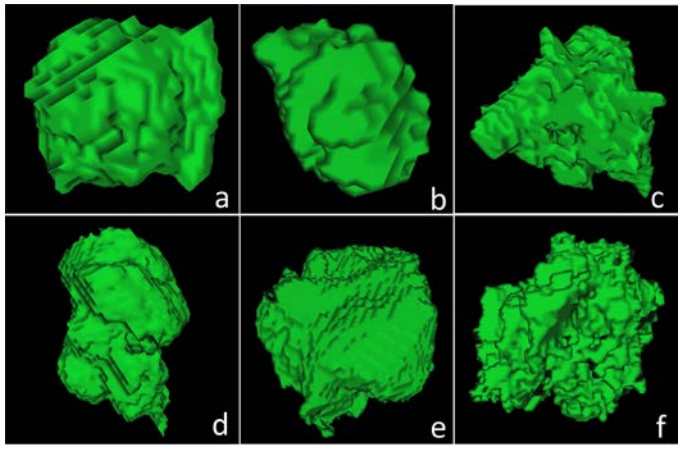

Fig. 20. Segmented lesions in 3D view. Images a, b, c, d, e, f show the lesions in P2, P7, P9, P10, P12, P17 respectively.

However, we achieved poor segmentation results in a few lung lesions. A case in point is the result on a solid nodule as shown in Fig. 21, where a(1) presents the TBGA result and a(2) describes the manual delineation. From the 161st slice to the 164th, the lesion by TBGA contains a neighboring vessel as the pixel intensity of the small part connecting the lesion and the vessel is too similar to distinguish. Another case is shown in Fig. 21(b), where b(1) presents the TBGA result and b(2) describes the manual delineation of GGO. The lesion segmented by TBGA comprises a highlighted vessel from the 163rd slice, as the pixel intensity of the region connecting the GGO and the vessel is close to them.

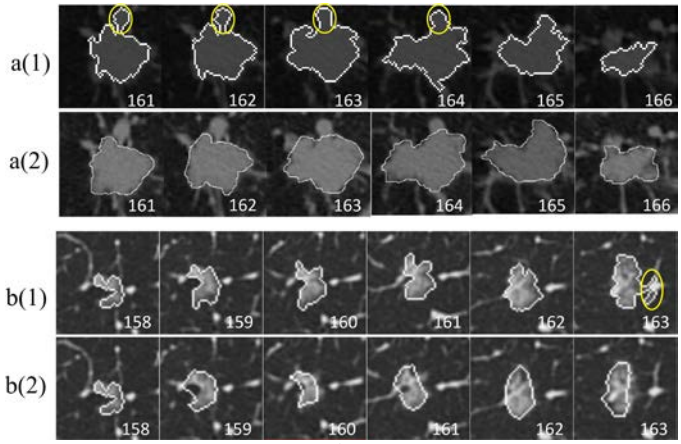

Fig. 21. Tumor segmentation results of a solid nodules a. (slices 161st–166th) and a GGO b. (slices 158th–163rd). a(1) and b(1) are the segmentation results by TBGA while a(2) and b(2) show the manual segmentation by R1. The vessels which have been included are circled by yellow in the figures.

IV. Discussion

The greatest contribution of our method is the three-steps framework for lung lesion segmentation. We presented an automatic method for the lung lesion seed point(s) initialization, and then the subsequent 3D lung lesion segmentation was performed without any training datasets or human interactions. The proposed method could achieve a high recognition rate of lung lesions, which have correctly identified 96.4% of the lesions with a specificity of 73 false positives in total on the lesions from the LIDC-IDRI dataset.

Another contribution is the segmentation of ground-glass

This article has been accepted for publication in a future issue of this journal, but has not been fully edited. Content may change prior to final publication. Citation information: DOI 10.1109/TMI.2015.2474119, IEEE Transactions on Medical Imaging

opacities. For the compared methods, the advantage of the LS algorithm from Li [43] is that it could depict the outline of GGO, as it is insensitive to the difference of pixel intensity. However, the lesion segmentation may not be completed if the number of evolution becomes less. SGC could access the lesion outline in a quicker response than the LS, but it is sensitive to juxta-vascular lesions. Our algorithm could find clearer lesion boundaries for ground-glass opacities without the disadvantages of time-consuming and easily included of blood vessels. An example is shown in Fig. 19, the LS method seems to achieve a similar result on GGO but the average of evolution for each slice is more than 1000. And neighboring vessels are involved by SGC approach from the 160th slice in Fig. 19. Besides, for the GGO attaches to the visceral pleura as shown in P17 described in Fig.18, the new algorithm delineates it well within 8.38 seconds. From the 41st slice, the new algorithm detects the boundary successfully where the nodule is connected to the pleura, which works much better than it did for solid nodules. In Table III, the average DC values of R1 vs. TBGA and R2 vs. TBGA on P14 to P19 (GGO) are 80.49% and 81.19% respectively. Compared with those values from LS and SGC in Table III, we can conclude that the new method works much better than LS and SGC on ground-glass opacities.

Finally, the new algorithm has the potential to provide a faster clinically aided diagnosis. Detailed description of computational cost has been presented as shown in the Section III-H. A segmentation example is shown in Fig. 16, all of the three methods could have good segmentation results compared with the radiologists' manual results (R1 and R2), because the spherical solid nodule is relatively easy to segment [14]. However, TBGA uses much less time than other methods as shown in Table V (the running time of TBGA, LS and SGC for this lesion is 4.72s, 15.00min and 25.30s respectively).

In terms of the evaluations on the LIDC-IDRI dataset and the clinical dataset, a conclusion could be made that the novel algorithm significantly improves lung lesion segmentation accuracy compared with other methods. Meanwhile, according to the comparison of TBGA vs. LS, TBGA vs. SGC and LS vs. SGC we find that the differences of these three methods are all significant ($P < 0.05$) in DC and HD. Different segmentation mechanisms are mainly responsible for this discrepancy. TBGA is voxel-based growing, but LS is based on the gradient and contour which tries to find the minimum of the energy function, while the SGC needs a pre-segmentation of the lung skeleton. We also compared the average of the two radiologists with these three methods. R is used to represent the average of R1 and R2. The DC values of R vs. TBGA, R vs. LS, and R vs. SGC is 80.28%, 65.70% and 68.60% respectively, which further illustrated that the results of the new algorithm are more accurate than those of LS and SGC. Similar results could be found by those comparisons using HD. Another conclusion could also be drawn is that our algorithm could obtain consistent results by different evaluation criteria such as DC and HD. All of these results demonstrate that the new method is more robust than the other methods.

In Table III and Table IV, we calculated *P* values of the *t*-test for each comparison with a reference to R1 vs. R2. The *P* values of R1 vs. TBGA and R2 vs. TBGA are much higher than 0.05 but the other *P* values are very small. Hence, we can conclude that there are significant differences between the results of other methods and manual segmentations (R1 and R2). But, for the proposed algorithm, the difference with manual segmentations is not statistically significant.

For the burrs on the outline of cavity, as shown in Fig. 10 and Fig. 11, the performance of burrs segmentation by TGBA is more superior to the manual one from slice 229th. As the manual drawing is always tedious, so the segmentation of burrs with our automatic method is more credible than the manual.

From Fig.13, an average DC value for TBGA vs. MBGA is much higher than 90%, which means that the automatic selection method of the seed point is robust and the segmentation is insensitive to the seed point position. The segmentation accuracy of some lesions could reach more than 90%. However, the accuracy on a few lesions is lower than 60% due to their specific morphology. Besides, the segmentation results by R1 vs. TBGA on the 115 lesions are more compact but the results of R1 vs. MBGA are fluctuant. So a conclusion could be summarized that the automatic seed selection method is credible as a stable segmentation result could be obtained by the proposed algorithm when the seed point(s) are selected automatically.

For the tissues connected to the adjacent lesion with similar intensity of pixels, a high degree of recognition is lacking by the proposed method. This is the main reason for the poor segmentations. Our future work will focus on the accurate boundary detection for juxta-pleural and juxta-vascular lesions. As for lesion segmentation, precise lung parenchyma segmentation is another issue we should address in the future. Generally, the segmentation result of lung parenchyma is the basis of lesion extraction, so the lung parenchyma should include the lesions wherever they located.

V. Conclusion

In this paper, we present an automatic, stable and quick-response lung lesion segmentation algorithm, which has been tested not only on the public LIDC-IDRI database but also on the clinical dataset. The initial seed points were first detected using an improved toboggan method for the subsequent 3D lesion segmentation. Then, the lesion was extracted by an automatic growing algorithm with multi-constraints. Finally, the segmentation result was optimized by a lung lesion refining method. The important component of this work is that it does not require any training datasets or human interactions (average (3+1+1)/3=1.70 interactions for SGC, SCES and LS) for lesion seed point detection, while it could obtain more accurate segmentation results compared with other methods, especially for ground-glass opacities. Besides, compared with the previous lung lesion segmentation algorithms, better performance was obtained with improved time efficiency by our method. As the new method has a variety of advantages for the segmentation of lung lesions, it will be further examined in clinical environment and can also be applied as a reference for lesion segmentation in other tissues.

This article has been accepted for publication in a future issue of this journal, but has not been fully edited. Content may change prior to final publication. Citation information: DOI 10.1109/TMI.2015.2474119, IEEE Transactions on Medical Imaging

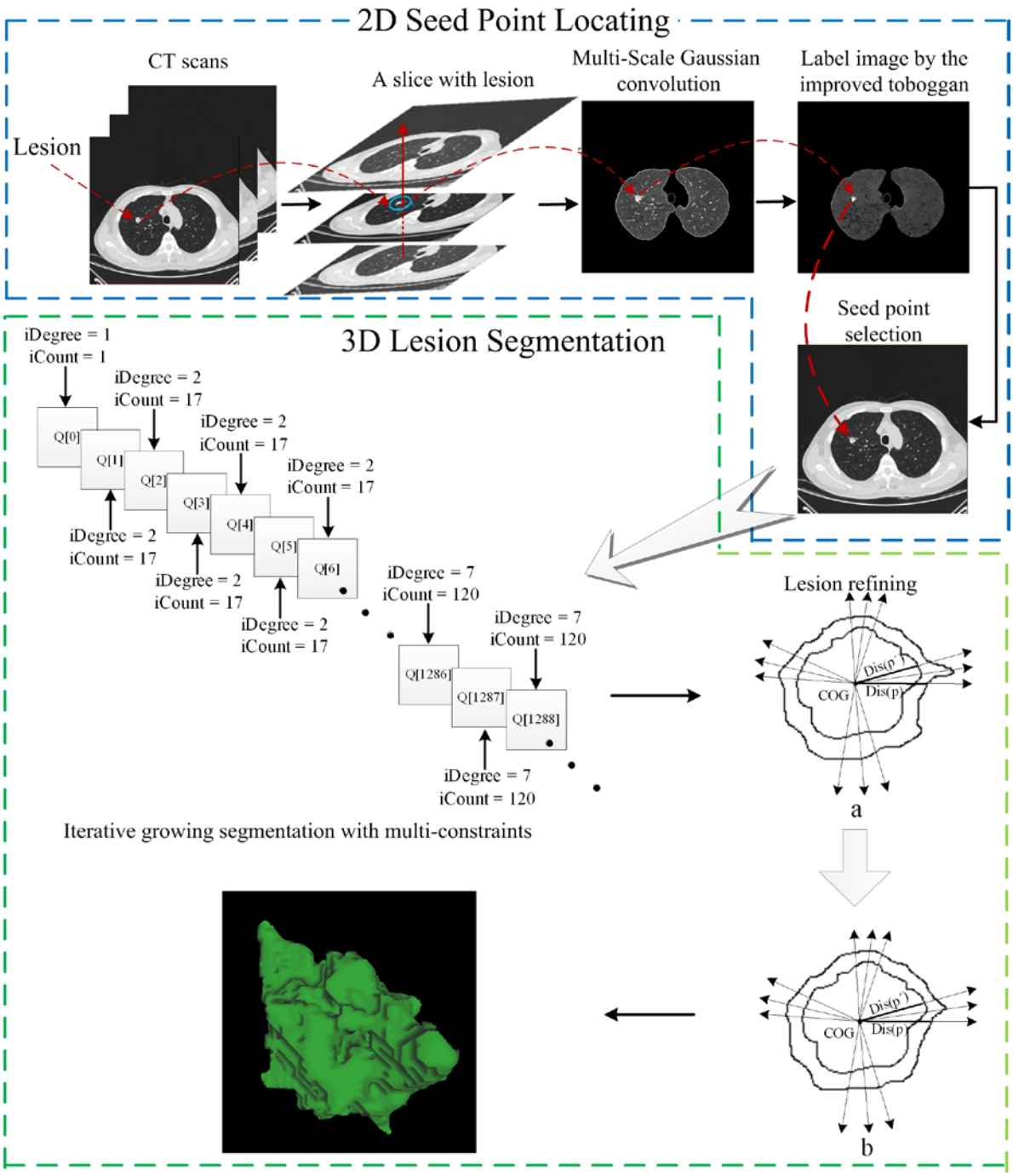

A detailed flowchart of the TBGA with figures for each section. The part in the blue frame is the seed point selection using the improved toboggan method, the part in the green one is the 3D lesion segmentation and final lesion refinement.

REFERENCES

[1] R. Siegel, D. Naishadham, and A. Jemal, "Cancer statistics, 2013," *CA Cancer J Clin*, vol. 63, pp. 11-30, Jan 2013.

[2] W. H. Organization, "Description of the global burden of NCDs, their risk factors and determinants," *Geneva, Switzerland: World Health Organization*, 2011.

[3] H. J. W. L. Aerts, E. R. Velazquez, R. T. H. Leijenaar, C. Parmar, P. Grossmann, S. Cavalho, J. Bussink, R. Monshouwer, B. Haibe-Kains, D. Rietveld, F. Hoebers, M. M. Rietbergen, C. R. Leemans, A. Dekker, J. Quackenbush, R. J. Gillies, and P. Lambin, "Decoding tumour phenotype by noninvasive imaging using a quantitative radiomics approach.," *Nat. Commun.*, vol. 5, p. 4006, 2014.

[4] J. Song, C. Yang, et al. "A New Quantitative Radiomics Approach for Non-Small Cell Lung Cancer (NSCLC) Prognosis." presented at the 101nd Int. Conf. Radiological Society of North America, Chicago, Illinois, November 29 - December 04, 2015.

[5] M. Nakata, H. Saeki, I. Takata, Y. Segawa, H. Mogami, K. Mandai, and K. Eguchi, "Focal ground-glass opacity detected by low-dose helical CT," *Chest*, vol. 121, no. 5, pp. 1464–1467, 2002.

[6] S. Candemir, S. Jaeger, K. Palaniappan, J. P. Musco, R. K. Singh, Z. Xue, A. Karargyris, S. Antani, G. Thoma, and C. J. McDonald, "Lung segmentation in chest radiographs using anatomical atlases with nonrigid registration," *IEEE Trans. Med. Imaging*, vol. 33, no. 2, pp. 577–590, 2014.

[7] Bian, Zijian, et al. "Accurate airway centerline extraction based on topological thinning using graph-theoretic analysis." *Bio-medical materials and engineering* 24.6 (2014): 3239-3249.

[8] B. Lassen, E. M. Van Rikxoort, M. Schmidt, S. Kerkstra, B. Van Ginneken, and J. M. Kuhnigk, "Automatic segmentation of the

pulmonary lobes from chest CT scans based on Fissures, Vessels, and Bronchi," *IEEE Trans. Med. Imaging*, vol. 32, no. 2, pp. 210–222, 2013.

[9] D. M. Campos, A. Simões, I. Ramos, and A. Campilho, "Feature-Based Supervised Lung Nodule Segmentation," no. Ci, pp. 23–26, 2014.

[10] S. Diciotti, G. Picozzi, M. Falchini, M. Mascalchi, N. Villari, and G. Valli, "3-D segmentation algorithm of small lung nodules in spiral CT images.," *IEEE Trans. Inf. Technol. Biomed.*, vol. 12, no. 1, pp. 7–19, 2008..

[11] S. G. Armato, G. McLennan, D. Hawkins, L. Bidaut, M. F. McNitt-Gray, C. R. Meyer, A. P. Reeves, B. Zhao, D. R. Aberle, C. I. Henschke, E. A. Hoffman, E. A. Kazerooni, H. MacMahon, E. J. R. Van Beeke, D. Yankelevitz, A. M. Biancardi, P. H. Bland, M. S. Brown, R. M. Engelmann, G. E. Laderach, D. Max, R. C. Pais, D. P. Y. Qing, R. Y. Roberts, A. R. Smith, A. Starkey, P. Batrah, P. Caligiuri, A. Farooqi, G. W. Gladish, C. M. Jude, R. F. Munden, I. Petkovska, L. E. Quint, L. H. Schwartz, B. Sundaram, L. E. Dodd, C. Fenimore, D. Gur, N. Petrick, J. Freymann, J. Kirby, B. Hughes, A. Vande Casteele, S. Gupte, M. Sallamm, M. D. Heath, M. H. Kuhn, E. Dharaiya, R. Burns, D. S. Fryd, M. Salganicoff, V. Anand, U. Shreter, S. Vastagh, B. Y. Croft, and L. P. Clarke, "The Lung Image Database Consortium (LIDC) and Image Database Resource Initiative (IDRI): a completed reference database of lung nodules on CT scans.," *Med. Phys.*, vol. 38, no. 2, pp. 915–931, 2011.

[12] S. Diciotti, S. Lombardo, M. Falchini, G. Picozzi, and M. Mascalchi, "Automated segmentation refinement of small lung nodules in CT scans by local shape analysis," *IEEE Trans. Biomed. Eng.*, vol. 58, no. 12 PART 1, pp. 3418–3428, 2011.

[13] D. Wu, L. Lu, J. Bi, Y. Shinagawa, K. Boyer, A. Krishnan, and M. Salganicoff, "Stratified learning of local anatomical context for lung nodules in CT images," in *Proceedings of the IEEE Computer Society Conference on Computer Vision and Pattern Recognition*, 2010, pp. 2791–2798.

[14] A. a Farag, H. E. A. El Munim, J. H. Graham, and A. a Farag, "A novel approach for lung nodules segmentation in chest CT using level sets.," *IEEE Trans. Image Process.*, vol. 22, no. 12, pp. 5202–13, 2013.

[15] S. Sun, Y. Guo, Y. Guan, and H. Ren, "Juxta-Vascular Nodule Segmentation Based on the Flowing Entropy and Geodesic Distance Feature," *Scientia Sinica(Informationis)*, vol. 61, pp. 1136-1146, 2013.

[16] Y. Gu, V. Kumar, L. O. Hall, D. B. Goldgof, C. Y. Li, R. Korn, C. Bendtsen, E. R. Velazquez, A. Dekker, H. Aerts, P. Lambin, X. Li, J. Tian, R. A. Gatenby, and R. J. Gillies, "Automated delineation of lung tumors from CT images using a single click ensemble segmentation approach," *Pattern Recognit.*, vol. 46, no. 3, pp. 692–702, 2013.

[17] C. Bendtsen, M. Kietzmann, R. Korn, P. D. Mozley, G. Schmidt, and G. Binnig, "X-Ray computed tomography: Semiautomated volumetric analysis of late-stage lung tumors as a basis for response assessments," *Int. J. Biomed. Imaging*, vol. 2011, 2011.

[18] M. Athelogou, G. Schmidt, A. Schäpe, M. Baatz, and G. Binnig, "Cognition Network Technology – A Novel Multimodal Image Analysis Technique for Automatic Identification and Quantification of Biological Image Contents," in *Imaging Cellular and Molecular Biological Functions*, 2007, pp. 407–422.

[19] Q. Wang, E. Song, R. Jin, P. Han, X. Wang, Y. Zhou, and J. Zeng, "Segmentation of lung nodules in computed tomography images using dynamic programming and multidirection fusion techniques.," *Acad. Radiol.*, vol. 16, no. 6, pp. 678–688, 2009.

[20] T. Kubota, A. K. Jerebko, M. Dewan, M. Salganicoff, and A. Krishnan, "Segmentation of pulmonary nodules of various densities with morphological approaches and convexity models," *Med. Image Anal.*, vol. 15, no. 1, pp. 133–154, 2011.

[21] A. Mansoor, U. Bagci, Z. Xu, B. Foster, K. N. Olivier, J. M. Elinoff, *et al.*, "A generic approach to pathological lung segmentation," *IEEE Trans Med Imaging*, vol. 33, pp. 2293-310, Dec 2014.

[22] S. Hu, E. a. Hoffman, and J. M. Reinhardt, "Automatic lung segmentation for accurate quantitation of volumetric X-ray CT images," *IEEE Trans. Med. Imaging*, vol. 20, no. 6, pp. 490–498, 2001.

[23] A. S. 3Rd and S. WF, "Automated lung segmentation for thoracic CT impact on computer-aided diagnosis," *Academic Radiology*, vol. 11, pp. 1011-1021, 2004..

[24] M. Kakar and D. R. Olsen, "Automatic segmentation and recognition of lungs and lesion from CT scans of thorax," *Comput. Med. Imaging Graph.*, vol. 33, no. 1, pp. 72–82, 2009..

[25] S. G. Armato, M. L. Giger, and H. MacMahon, "Automated detection of lung nodules in CT scans: preliminary results.," *Med. Phys.*, vol. 28, no. 8, pp. 1552–1561, 2001.

[26] A. Madabhushi and D. N. Metaxas, "Combining low-, high-level and empirical domain knowledge for automated segmentation of ultrasonic breast lesions," *IEEE Trans. Med. Imaging*, vol. 22, no. 2, pp. 155–169, 2003.

[27] K. Murphy, B. van Ginneken, a. M. R. Schilham, B. J. de Hoop, H. a. Gietema, and M. Prokop, "A large-scale evaluation of automatic pulmonary nodule detection in chest CT using local image features and k-nearest-neighbour classification," *Med. Image Anal.*, vol. 13, no. 5, pp. 757–770, 2009.

[28] T. Messay, R. C. Hardie, and S. K. Rogers, "A new computationally efficient CAD system for pulmonary nodule detection in CT imagery," *Med. Image Anal.*, vol. 14, no. 3, pp. 390–406, 2010.

[29] B. Golosio, G. L. Masala, A. Piccioli, P. Oliva, M. Carpinelli, R. Cataldo, P. Cerello, F. De Carlo, F. Falaschi, M. E. Fantacci, G. Gargano, P. Kasae, and M. Torsello, "A novel multithreshold method for nodule detection in lung CT.," *Med. Phys.*, vol. 36, no. 8, pp. 3607–3618, 2009.

[30] M. Tan, R. Deklerck, B. Jansen, M. Bister, and J. Cornelis, "A novel computer-aided lung nodule detection system for CT images," *Med. Phys.*, vol. 38, no. 10, p. 5630, 2011.

[31] J. Fairfield, "Toboggan contrast enhancement for contrast segmentation," *[1990] Proceedings. 10th Int. Conf. Pattern Recognit.*, vol. i, pp. 712–716, 1990.

[32] E. N. Mortensen and W. a. Barrett, "Toboggan-based intelligent scissors with a four-parameter edge model," *Proceedings. 1999 IEEE Comput. Soc. Conf. Comput. Vis. Pattern Recognit. (Cat. No PR00149)*, vol. 2, pp. 452–458, 1999.

[33] H. Ibrahim, M. Petrou, K. Wells, S. Doran, and O. Olsen, "Preprocessing for use in automatic volumetric liver segmentation from NMR data," *IEEE Symp. Conf. Rec. Nucl. Sci. 2004.*, vol. 5, no. C, pp. 2783–2787, 2004.

[34] Y. C. Lin, Y. P. Tsai, Y. P. Hung, and Z. C. Shih, "Comparison between immersion-based and toboggan-based watershed image segmentation," *IEEE Trans. Image Process.*, vol. 15, no. 3, pp. 632–640, 2006.

[35] C. J. Armstrong, B. L. Price, and W. a. Barrett, "Interactive segmentation of image volumes with Live Surface," *Comput. Graph.*, vol. 31, no. 2, pp. 212–229, 2007.

[36] Tan, W., Yang, J., Bian, Z., Gong, Z., & Zhao, D. (2014). "Automatic extraction of 3d airway tree from multislice computed tomography images." *Journal of Medical Imaging & Health Informatics*, volume 4, 768-775(8).

[37] N. Baka, C. T. Metz, C. J. Schultz, R. J. Van Geuns, W. J. Niessen, and T. Van Walsum, "Oriented Gaussian mixture models for nonrigid 2D/3D coronary artery registration," *IEEE Trans. Med. Imaging*, vol. 33, no. 5, pp. 1023–1034, 2014.

[38] W. K. Moon, Y.-W. Shen, M. S. Bae, C.-S. Huang, J.-H. Chen, and R.-F. Chang, "Computer-aided tumor detection based on multi-scale blob detection algorithm in automated breast ultrasound images.," *IEEE Trans. Med. Imaging*, vol. 32, no. 7, pp. 1191–200, 2013.

[39] D. S. Paik, C. F. Beaulieu, G. D. Rubin, B. Acar, R. B. Jeffrey, J. Yee, J. Dey, and S. Napel, "Surface normal overlap: A computer-aided detection algorithm with application to colonic polyps and lung nodules in helical CT," *IEEE Trans. Med. Imaging*, vol. 23, no. 6, pp. 661–675, 2004.

[40] H. Wang, D. B. Stout, and A. F. Chatziioannou, "Estimation of mouse organ locations through registration of a statistical mouse atlas with micro-CT images," *IEEE Trans. Med. Imaging*, vol. 31, no. 1, pp. 88–102, 2012.

[41] M. Rajchl, J. Yuan, J. White, E. Ukwatta, J. Stirrat, C. Nambakhsh, F. Li, and T. Peters, "Interactive Hierarchical Max-Flow Segmentation of Scar Tissue from Late-Enhancement Cardiac MR Images.," *IEEE Trans. Med. Imaging*, vol. 33, no. 1, pp. 159–172, 2013.

[42] D. Mahapatra, P. J. Schüf, J. a W. Tielbeek, J. C. Makanyanga, J. Stoker, S. a Taylor, F. M. Vos, and J. M. Buhmann, "Automatic Detection and Segmentation of Crohn ' s Disease Tissues From Abdominal MRI," *IEEE Trans. Med. Imaging*, vol. 32, no. 12, pp. 2332–2347, 2013.

[43] C. Li, R. Huang, Z. Ding, J. C. Gatenby, D. N. Metaxas, and J. C. Gore, "A level set method for image segmentation in the presence of intensity inhomogeneities with application to MRI," *IEEE Trans. Image Process.*, vol. 20, no. 7, pp. 2007–2016, 2011.

[44] D. Xiang, J. Tian, F. Yang, Q. Yang, X. Zhang, Q. Li, and X. Liu, "Skeleton Cuts-An Efficient Segmentation Method for Volume Rendering," *IEEE Trans. Vis. Comput. Graph.*, vol. 17, no. 9, pp. 1295–1306, 2011.

[45] J. Tian, J. Xue, Y. Dai, J. Chen, and J. Zheng, "A novel software platform for medical image processing and analyzing," *IEEE Trans. Inf. Technol. Biomed.*, vol. 12, no. 6, pp. 800–812, 2008.